Optical Fiber Sensor Network and Industrial Applications

47

Qizhen Sun, Zhijun Yan, Deming Liu, and Lin Zhang

Contents

Abstract

For many of sensing applications, multiplexed sensor networks which can map the sensing signal of a large structure or surveying at complex conditions are required, greatly promoting the development of the fiber optic sensor network with large capacity. In this chapter, three typical fiber optic sensor networks

Q. Sun (✉) · Z. Yan · D. Liu
School of Optical and Electronic Information, Next Generation Internet Access National Engineering Laboratory (NGIAS), Huazhong University of Science and Technology, Wuhan, Hubei, P. R. China
e-mail: qzsun@mail.hust.edu.cn

L. Zhang
Aston Institute of Photonic Technologies, Aston University, Birmingham, UK

G.-D. Peng (ed.), *Handbook of Optical Fibers*,
https://doi.org/10.1007/978-981-10-7087-7_20

and their applications will be introduced. Firstly, the ultra-weak fiber Bragg grating (UWFBG) sensor networks with ultra-large capacity for quasi-distributed and continuous distributed sensing in a single fiber link are investigated, which is realized by the multiplexing of UWFBGs or UWFBG based Fabry-Parot interferometers (FPI). Secondly, special fiber grating sensor networks with advanced functions and competitive performances, including the tilted fiber grating (TFG) sensors or distributed Bragg grating fiber laser (DBRFL) sensors multiplexed in a single fiber, are investigated. Thirdly, fiber optic sensors passive optical networks (SPON) with good adaptability, high extendibility, and great flexibility are comprehensively studied, which includes the star topology SPON and the tree topology SPON for colored sensors and colorless sensors accessing. For each type of sensor network, the sensor structures, networking mechanisms, system architectures, demodulation methods, and typical sensing performances are systematically discussed. Moreover, the developed systems or equipment and field tests for a wide range of commercial and industrial applications, especially for resource exploration, geophysics, infrastructure, medical diagnosis, food quality, and security control, are presented.

Keywords
Fiber optic sensor network · Fiber grating sensor network · Fiber optic distributed sensing · Senor passive optical network

Introduction

Due to the distinct advantages of light weight, small size, high sensitivity, immunity to electromagnetic interference, and ease to network, there is a high demand for smart optical fiber sensor technologies due to increasingly application needs in a wide range of sectors, including civil engineering, aerospace, maritime, energy, and defense industries, as well as in medical, environmental, and food sectors. Recent market analysis by ElectroniCast has reported that the global market value for fiber optic sensors was projected to $3.38 billion in 2016 and will increase to more than $5.98 billion in 2026 (ElectroniCast consultants 2017). For many of sensing applications, multiplexed sensor networks which can map the sensing signal of a large structure (e.g., oil-gas well, pipeline, bridge, border, aircraft wing, etc.) or geophysical surveying at complex conditions are required, for which single or pairs of sensors are not sufficient. Therefore, the fiber optic sensor network with large capacity is becoming an inevitable tendency for the sensing industry.

The fiber optic sensor network mainly includes point fiber sensor array and distributed fiber sensor system, of which the sensor units can be multiplexed by specific schemes, including time division multiplexing (TDM), wavelength division multiplexing (WDM), frequency division multiplexing (FDM), space division multiplexing (SDM), or their combinations. Apart from seeing many successful commercial deployments of fiber sensors, novel and function-enhanced fiber sensors have been developed by utilizing specially modified structures and speciality fibers.

In this chapter, three typical fiber optic sensor networks will be introduced, including the ultra-weak fiber Bragg grating (UWFBG) sensor network (section "Ultra-Weak Fiber Bragg Grating (UWFBG) Sensor Network and Applications"), special fiber grating sensor network (section "Special Fiber Grating Sensor Network and Applications"), and fiber optic sensors passive optical network (SPON) (section "Fiber Optic Sensors Passive Optical Network (SPON) and Applications"). The sensor structures, networking mechanisms, system architectures, demodulation methods, and the sensing performances will be discussed. Moreover, a wide range of industrial applications, especially for resource exploration, geophysics, infrastructure, medical diagnose, food quality, and security control will be presented.

Ultra-Weak Fiber Bragg Grating (UWFBG) Sensor Network and Applications

Over the last decade, one of the most versatile and broadly researched and developed optical fiber sensor platforms is the in-fiber gratings, owing that the modulation pattern of the refractive index (RI) in fiber grating is sensitive to external parameters such as temperature, strain, and surrounding RI, resulting in the nominal wavelength shift. Until now, fiber Bragg gratings written on standard fiber have been widely used for measuring temperature, strain and force, pressure, vibration, liquid level, displacement, twist and torsion, bending and loading, current and magnetic field, chemicals and biochemical, etc., which are showing great potential and broad market prospects in industrial fields.

The wavelength encoded nature of the information facilitates WDM for sensor networking, achieved by assigning individual sensors to a different slice of the available source spectrum (Fallon 2000), as illustrated in Fig. 1. This outstanding advantage makes fiber gratings become ideal candidates for many applications. Except for WDM, FBG can also be multiplexed by TDM or the combination of them to build a sensor network along one fiber for large area measurement.

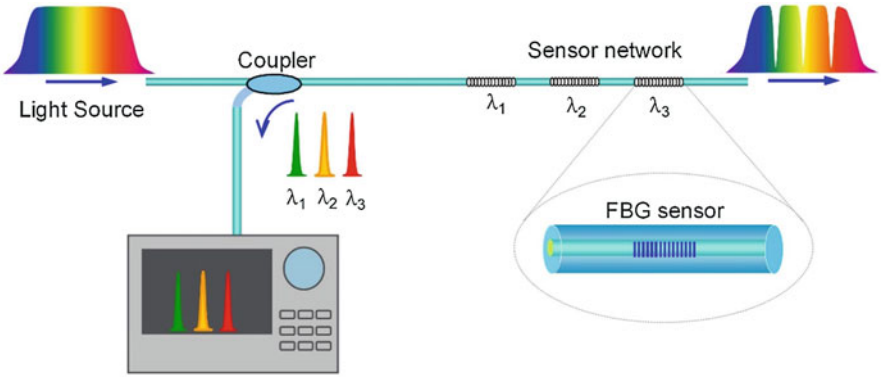

Fig. 1 Schematic of the fiber grating sensor network

However, the insertion loss induced by number of the FBGs is high, and therefore, the multiplexing capacity is limited to be about several hundreds, typically less than 100. Recently, UWFBG -based sensor network was proposed and investigated. The reflectivity of FBG is smaller than 1%, even decreased to about 10^{-5}, so the insertion loss into the fiber can be ignored. Consequently, there is enormous potential in the multiplexing capacity along single fiber. In this section, four types of UWFBG-based sensor network and the typical applications will be discussed.

TDM-Based Quasi-Distributed Sensor Network

Based on the narrow bandwidth and weak reflectivity of UWFBG, identical gratings can be multiplexed in time domain to improve the multiplexing capacity and sensing distance greatly. Figure 2a presents the working principle of the identical UWFBG multiplexed sensor network for quasi-distributed sensing. When pulse signal incidents into the fiber, a pulse sequence will be reflected and different pulse corresponds to different UWFBGs. Meanwhile, the central wavelength of the reflected pulse presents the value of the sensing parameter of it. It means that the UWFBG sensors can be interrogated in both time domain and wavelength domain, achieving multi-point synchronous precision measurement and positioning. The propagation of the optical wave in the fiber is similar with the backscattering of fiber, such as Rayleigh scattering, Brillion scattering and Raman scattering which can implement long distance and distributed sensing. Hence the sensing system is named as the microstructure-OTDR, i.e., M-OTDR, because the UWFBGs can be considered as longitudinal distributed microstructures. While the reflectivity of the UWFBG is several orders of magnitude higher than backscattering light as shown in Fig. 2b, it is a perfect candidate for improving the signal to noise ratio (SNR) of the backscattering light in fiber as the sensing point, resulting in the higher measurement precision and greatly shorter response time. Meanwhile, by networking the identical UWFBGs through TDM, the multiplexing capacity in a single fiber can be greatly improved to 1000 due to the relatively lower insertion loss (Zhang et al. 2012a). Along with the decrease of the UWFBG reflectivity, the effect of the cross-talk induced by multi-reflection between the gratings will be weakened gradually (Hu et al. 2014). When the UWFBG reflectivity is about −40 dB with the central wavelength of 1550.9 nm, the multiplexed number of gratings could reach up to1642, showing a low transmission loss (Wang et al. 2016).

Owing to the advantages of large multiplexing capacity, high measurement accuracy, and long-sensing distance, this sensing network has a great potential for health monitoring of bridges, dams, tunnels, and other distributed sensing applications. For example, the network made up of 6108 UWFBGs with two wavelength bands in a 10 km fiber was developed and the distributed temperature measurement was conducted by using a temperature test chamber. The experimental results were shown in Fig. 3, exhibiting the red shift of peak wavelength with the increase of temperature, measurement accuracy of 0.5 °C, and good linear response with the coefficient around 10.68 pm/°C at any gratings (Yang et al. 2016).

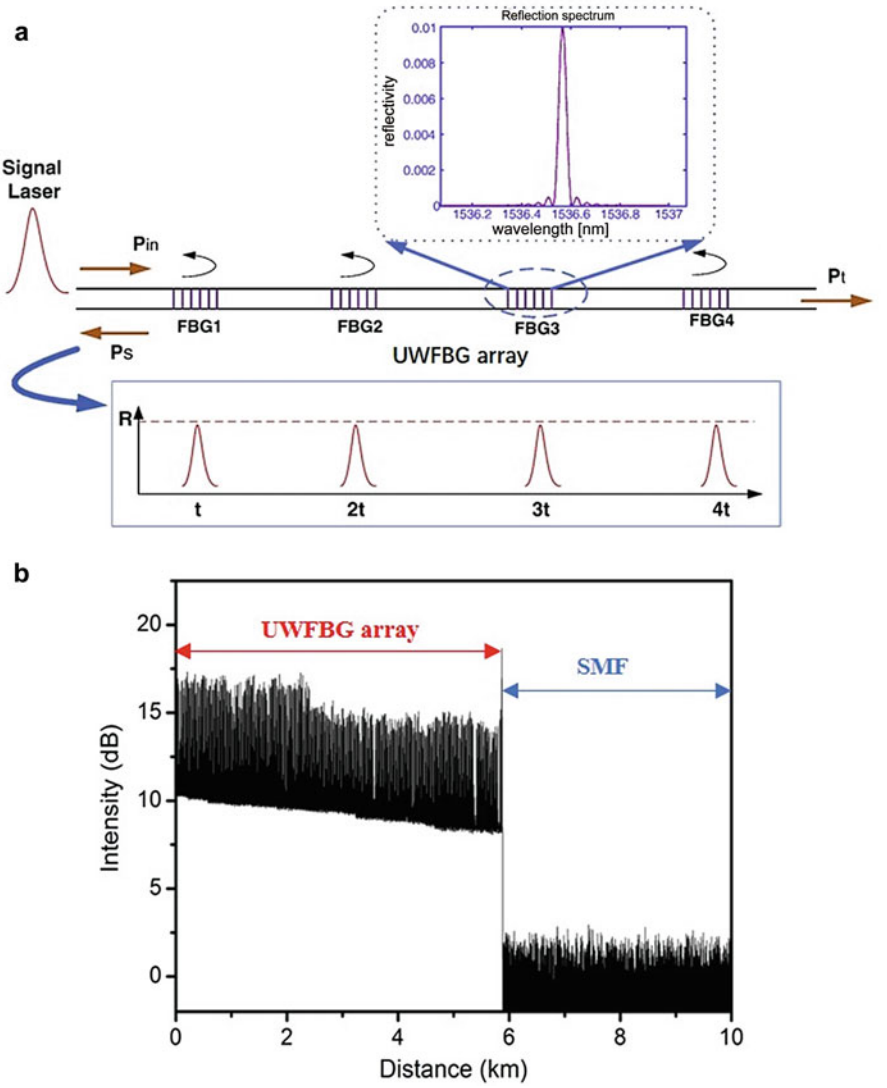

Fig. 2 Schematic of the identical UWFBG multiplexed sensor network: (**a**) working principle; (**b**) OTDR trace of the UWFBG array. (Copyright 2019 Springer)

TDM-Based Continuous-Distributed Sensor Network

Although high SNR can be realized with UWFBG, fiber between two neighboring UWFBGs becomes dead zone of the sensing system. To detect the event occurred in this section, the UWFBGs based fiber as the sensing link and the coherent OTDR as the demodulation scheme were combined to realize wideband

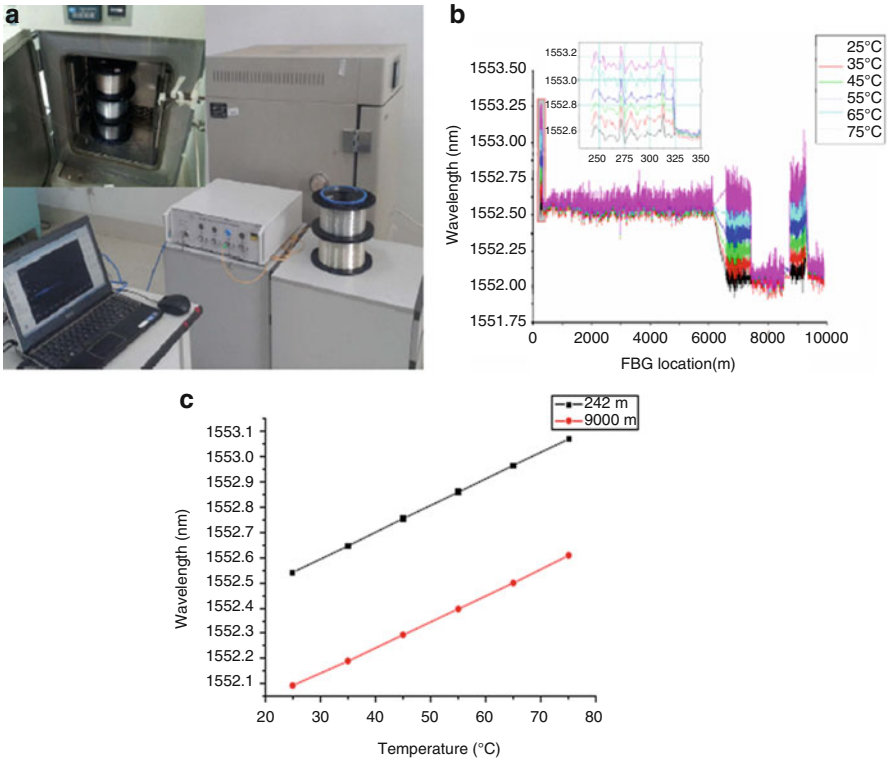

Fig. 3 Experimental demonstration: (**a**) images of the interrogation system of an UWFBG array, (**b**) temperature sensing performance of the UWFBG array, and (**c**) the temperature response of two UWFBGs located 242 and 9000 m. (Copyright 2019 Springer)

and high sensitive fully-distributed sensing. As illustrated in Fig. 4, light from the laser source is modulated into pulses and frequency shifted by Δf after passing through the acoustical optical modulator (AOM). After amplified by EDFA and filtering process, reflected pulses from the UWFBG are combined with the local oscillator and received by the balanced photo detector (BPD). The reflected signal contains the intensity and the phase information of every UWFBG. Phase change on the sensing fiber induced by external parameters is obtained by calculating the phase difference between every two adjacent UWFBGs through differential cross-multiplying (DCM) algorithm. And the event location is identified by searching the peaks of the backscattered light; therefore, the spatial resolution is determined by spatial interval of UWFBGs (Ai et al. 2017).

Based on the above setup, distributed vibration, acoustic wave, strain, and temperature, detection were explored. Specifically, as the phase change induced by the temperature and the vibration event would occupy different frequency band, after the low pass filter (LPF) and the high pass filter (HPF), the vibration and temperature

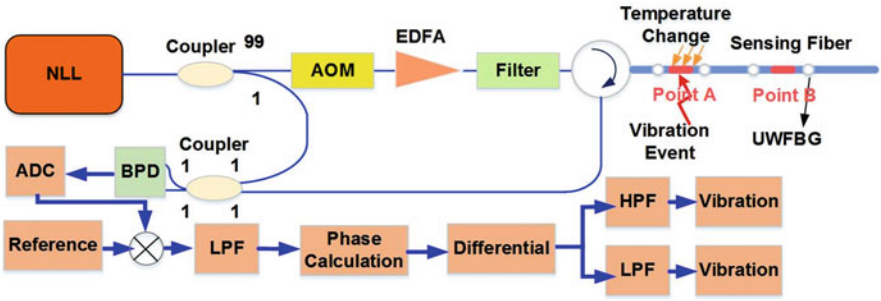

Fig. 4 Configuration of the distributed sensing system based on UWFBGs sensing link. (Copyright 2019 OSA)

change can be measured simultaneously (Ai et al. 2018). The experimental results are displayed in Fig. 5, which demonstrate that the sensor system can accurately map the temperature distribution and trace the multiple vibrations along the sensing fiber, as well as simultaneously detect the temperature change and vibration signal occurred at the same position of 752 m.

In addition, the sensor network provides excellent sensing performance for distributed acoustic sensing (DAS) with wideband covering from static to ultrasonic range. When no strain was applied on the sensing fiber, phase noise spectral densities at low frequency and high frequency were recorded and presented in Fig. 6a, b. It is clear that the phase noise above 1 Hz is as low as 7×10^{-4} rad, which means that the system can respond to the acoustical signal at ultra-low frequency region. To evaluate the sensitivity to acoustical waves, static strain test was conducted. As shown in Fig. 6c, sensitivity of 4.393 rad/$\mu\varepsilon$ as well as good linear relationship with $R^2 > 0.9998$ were achieved. From the phase noise spectral density above, the strain resolution over 1 Hz can be deduced to be lower than 0.16 nε. Meanwhile, the demodulated acoustic distribution along the sensing fiber was investigated. The experimental results in Fig. 7a, b prove that the DAS system owned wide response band from 0.1 Hz to 45 kHz, with successful recovery of the acoustic wave.

It should be emphasized that not only the UWFBG with certain wavelength selection but also the ultra-weak chirped FBG(UWCFBG) with wideband selection or the local abrupt change point of RI without wavelength selection can be served as the backscattering enhanced microstructure, which are inscribed in the fiber through UV or femtosecond lasers exposure.

The M-OTDR based DAS system have been widely applied in industrial fields such as borehole survey (Yamate et al. 2017; Mateeva et al. 2014), seismic recording (Ni et al. 2005; Jousset et al. 2018), and rail crack detection (Fan et al. 2019). Figure 8 presents our field test conducted in an oilfield (Fig. 8a). A 1 km long UWFBG array fiber cable was deployed into a cased borehole with a weight bar to pull the fiber cable down to the borehole (Fig. 8b). An explosive source was used to generate seismic energy on the surface with different

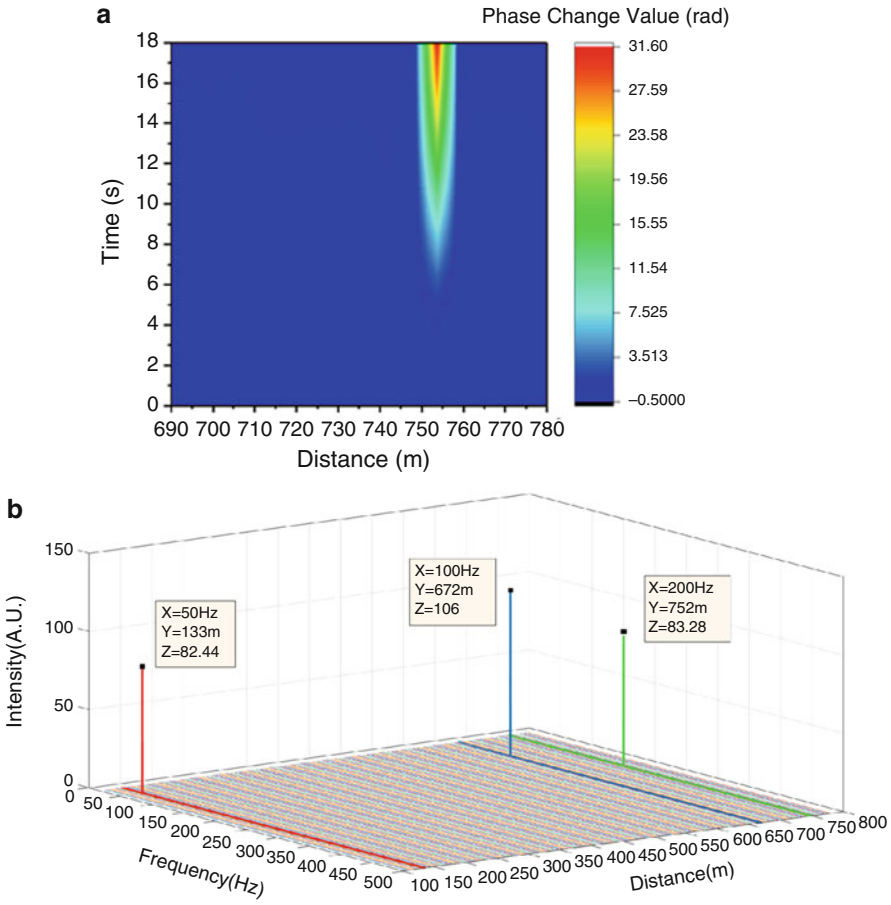

Fig. 5 Experimental results of simultaneous temperature and vibration measurement for UWFBG array based full-distributed sensor network: (**a**) phase distribution along the sensing fiber when the temperature at Point A changes; (**b**) vibration frequency distribution along the sensing fiber when multiple vibrations were applied on different positions

offset distance to the wellhead. From Fig. 8c, it can be seen that the fiber DAS system based on UWFBG sensor network acquired borehole seismic data with good quality, where both of the upgoing wave and downgoing wave can be clearly detected.

Figure 9 illustrates the field test of fiber DAS system to record seismic data. From Fig. 9a–c, it can be seen that the distance between the seismic signal and the seismometer or DAS system is about 8.7 km, and 500 m SNR enhanced sensing fiber cable was buried underground with the depth of about 20 cm to record the seismic wave transmission. Figure 9d clearly shows the excited wave by heavy hammer near the fiber, and the comparison of the recorded seismic data

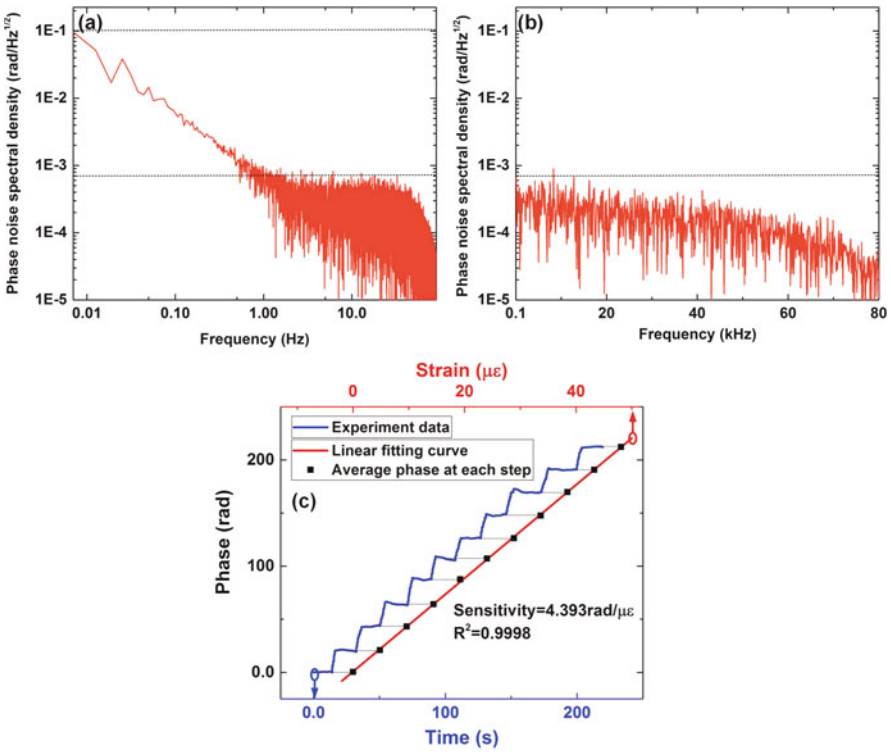

Fig. 6 Noise floor and sensitivity of UWFBG array fiber based DAS: (**a**) phase noise spectral density of low frequency less than 10 Hz; (**b**) phase noise spectral density from 0.1 to 80 kHz; (**c**) relationship between phase change and applied strain

from electrical seismometer and fiber DAS in Fig. 9f demonstrates that the fiber DAS can detect the seismic data with high sensitivity, high accuracy as well as wider response frequency band. In addition, as presented in Fig. 9e, the fiber DAS system successfully recorded the vehicle movements in this area all the time, which can used for analyzing the traffic condition and the noise pollution in the city.

Figure 10 shows our application test for rail crack detection, where the UWFBG array fiber cable was laid on rail waist (i.e., in the middle of the rail track, which is also called rail web) (Fig. 10a). When the train went through a crack on the rail, a strong acoustic source was excited at this position owing to the interaction between the wheels and uneven rail, and then propagated both in forward and backward directions. As depicted in Fig. 10b, c, by analyzing the temporal and spatial distribution of sound waves recorded by the DAS system, the intersection point of the forward and backward wave propagation traces can be found, which corresponds to the accurate location of the crack. The method has great prospect in enhancing railway safety.

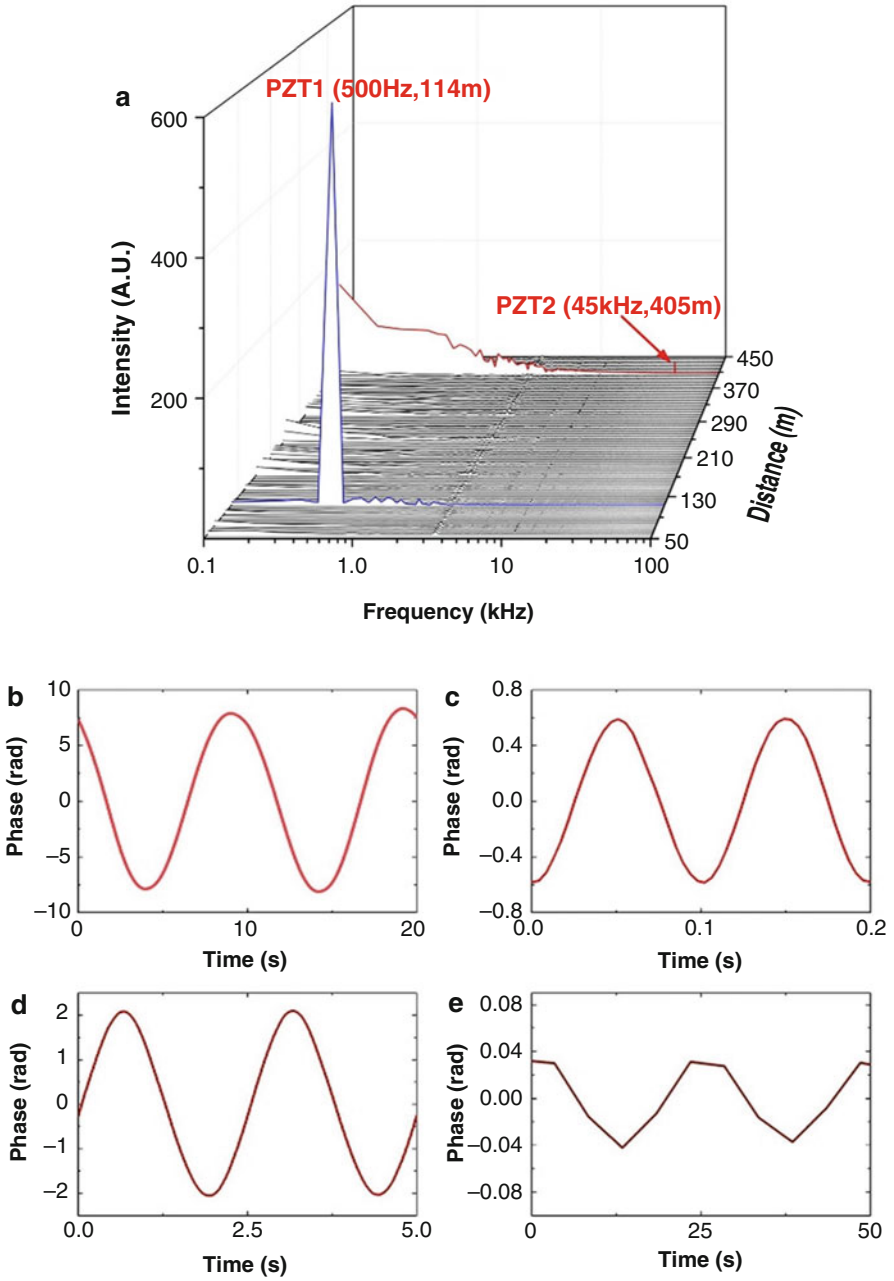

Fig. 7 Acoustic sensing performance of UWFBG array fiber based DAS: (**a**) the frequency spectrum along the fiber when 500 Hz and 45 kHz acoustic signals were applied through PZTs; demodulated waveform of acoustic signal with frequency of (**b**) 0.1 Hz; (**c**) 10 Hz; (**d**) 400 Hz; (**e**) 40 kHz

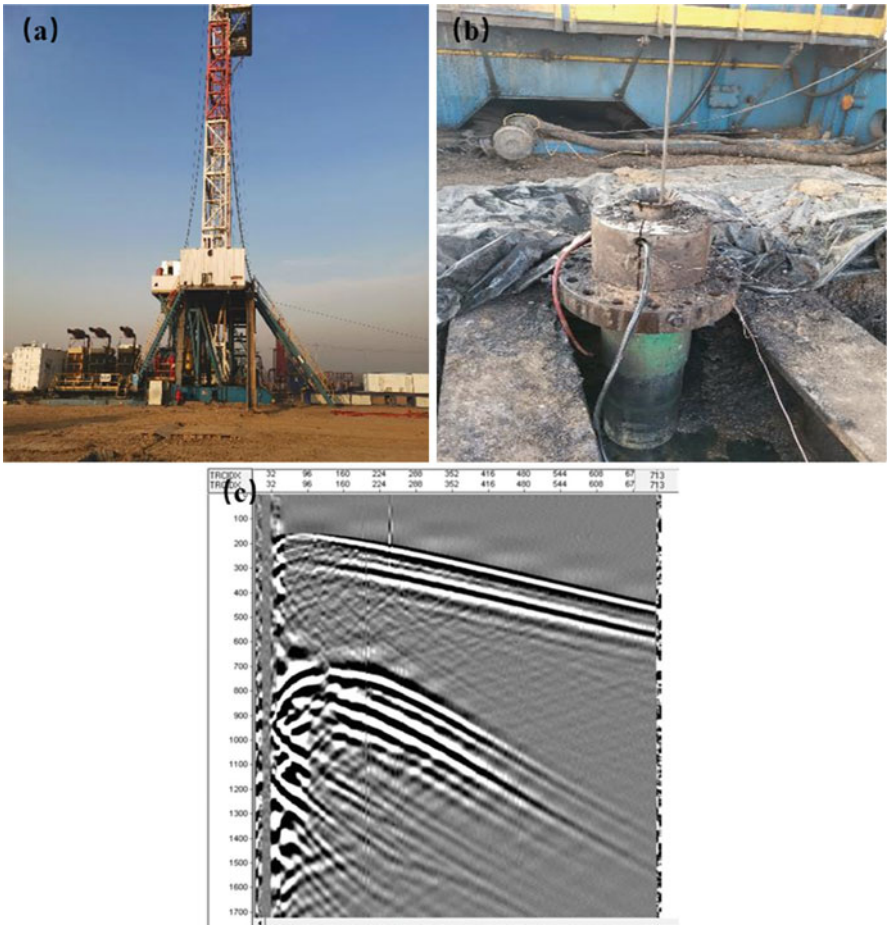

Fig. 8 Field test of borehole survey: (**a**) photograph of the well site; (**b**) photograph of the borehole and fiber cable; (**c**) recorded borehole seismic data excited by explosive source

WDM/FDM-Based Quasi-Distributed Sensor Network with High Spatial Resolution

The locating principle in TDM scheme described above is still based on the time delay tracking, so the spatial resolution is relatively larger than 1 m, which is not enough for special applications. In order to further increase the multiplexing capacity and improve the spatial resolution of the UWFBG sensor network, a fiber microstructure as shown in Fig. 11a was proposed and designed, which can be considered as Fabry-Pérot interferometer (FPI) composed of two closely spaced UWFBGs. Owing to the weak reflectivity of the gratings, one microstructure can be considered as a low-finesse FPI, of which the reflectivity R_S can be simplified as a

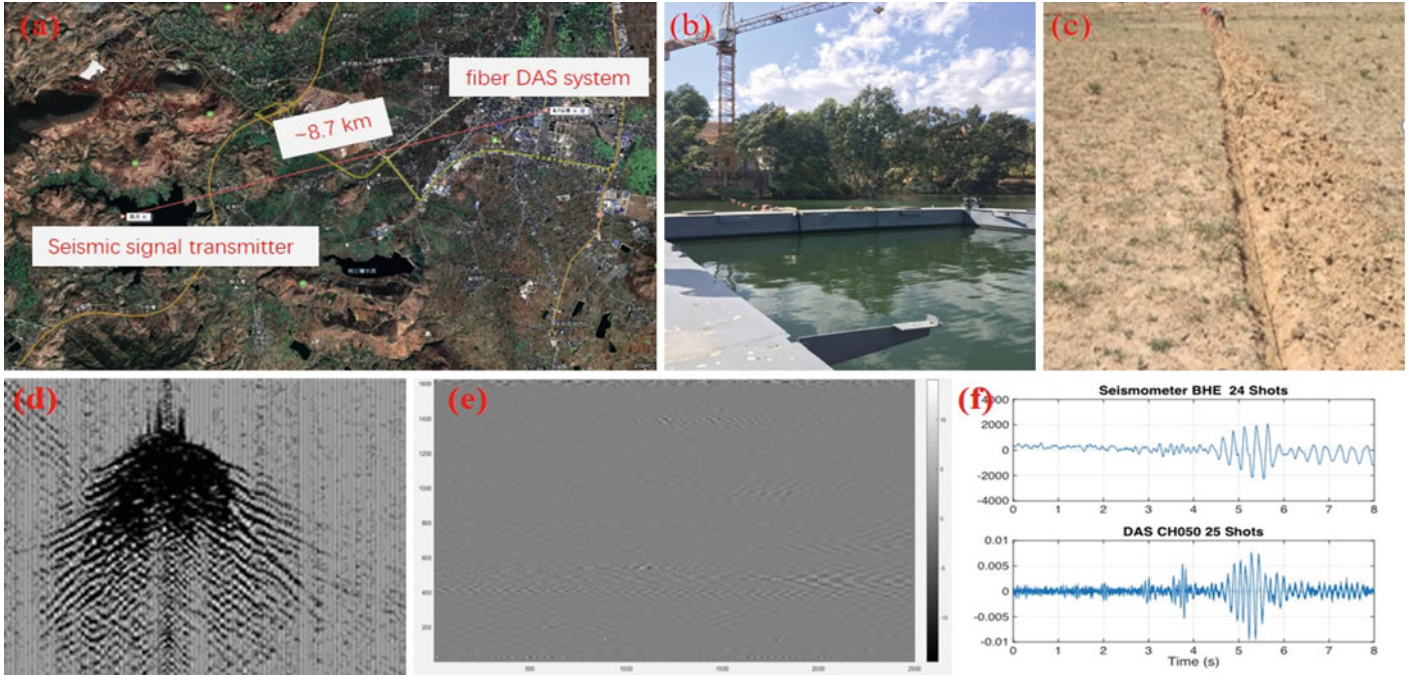

Fig. 9 Field test of seismic recording: (**a**) google map of the test site, where the distance between the seismic signal transmitter and the fiber DAS system is about 8.7 km; (**b**) photograph of the seismic signal transmitter; (**c**) photograph of the shallow buried sensing fiber cable; (**d**) recorded seismic data excited by heavy hammer signal near the fiber cable; (**e**) recorded seismic data excited by vehicle movements; (**f**) comparison of the recorded seismic data from electrical seismometer and fiber DAS, which was excited by the distant seismic signal transmitter

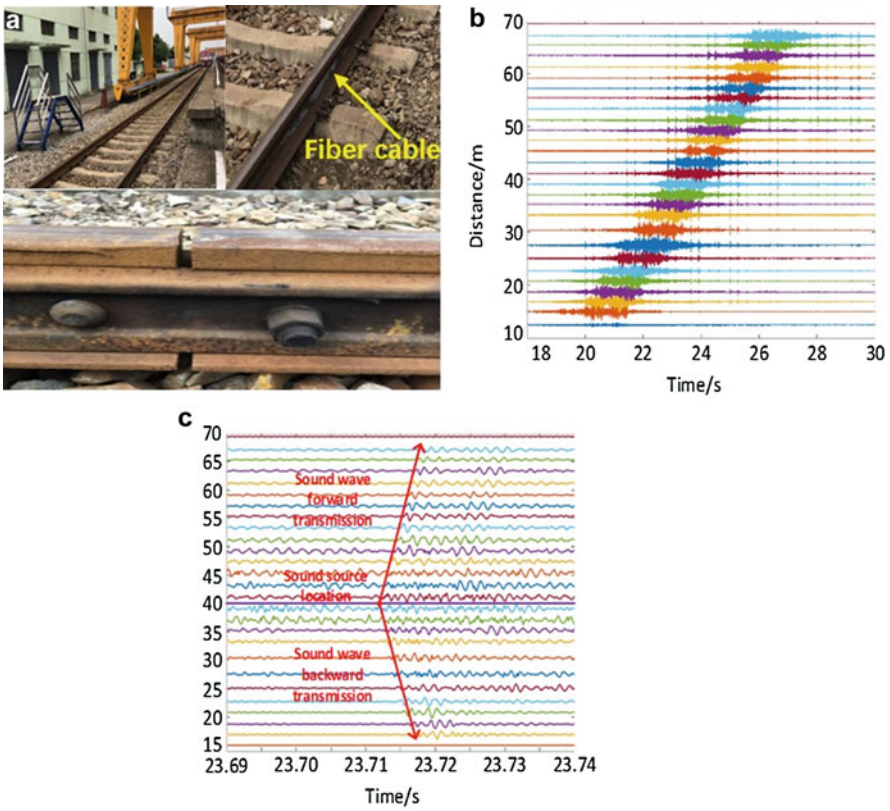

Fig. 10 Field test of railway monitoring: (**a**) photographs of the railway attached with fiber cable and crack on the track; (**b**) acoustic wave distribution along the railway measured by fiber DAS system; (**c**) Zoom of certain section in (**b**) after filtering. (Copyright 2019 OSA)

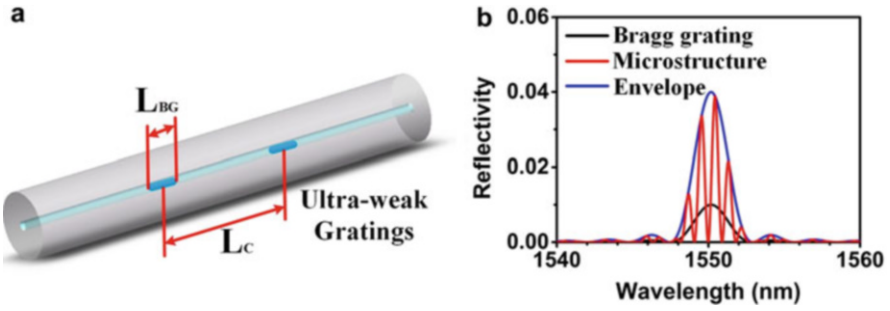

Fig. 11 (**a**) The configuration of the microstructure; (**b**) the reflection spectrum. (Copyright 2019 OSA)

two-beam interferometer (Miridonov et al. 1998):

$$R_S = 2R_G\left[1 + \cos\left(4\pi n_{\text{eff}} L_C/\lambda\right)\right] \tag{1}$$

where n_{eff} is the effective refractive index, L_C is the cavity length of the microstructure, R_G is the reflectivity of the UWFBG, and λ is the operating wavelength. The free spectral range (FSR) of the resonant peak, determined by L_C, is associated with the frequency v_c of the microstructures in the Fourier frequency domain:

$$v_c = \frac{2n_{\text{eff}} L_C}{{\lambda_B}^2} \tag{2}$$

The backward scattering spectrum R_S of the microstructure is an UWFBG envelop modulated by F-P comb filtering as depicted in Fig. 11b, which is related to the Bragg wavelength λ_B and the frequency v_c. Therefore, the microstructures can achieve wavelength and frequency encoding simultaneously (Zhang et al. 2019).

The multiplexing capacity of the microstructures is analyzed for high spatial resolution distributed sensing, which can be calculated through the number of WDM channels and FDM channels as follows:

$$N = N_{\text{WDM}} \cdot N_{\text{FDM}} = \frac{\delta\lambda_s}{\delta\lambda_B} \cdot \frac{L_m}{\Delta L_C} = \frac{n_{\text{eff}}\delta\lambda_s L_m}{2{\lambda_B}^2} \tag{3}$$

Where $\delta\lambda_B$ is the operating bandwidth of the microstructures, L_m and ΔL_C are respectively the maximum cavity length of the microstructure and the cavity length difference between the microstructures in adjacent FDM channels, and $\delta\lambda_s$ is the bandwidth of the interrogation system. Theoretically, over 1000 microstructures with spatial interval less than 1 cm can be high-densely multiplexed along the single fiber (Li et al. 2012a).

In order to achieve high resolution and fast response, a demodulation system is developed by combining the fiber Fabry-Perot tunable filter (FFP-TF) tuning with a parallel signal processing algorithm. As shown in Fig. 12, the parallel processing flow of demodulation scheme contains four parts. Firstly, the modulated optical signal from the sensor array is scanned using a FFP-TF controlled synchronously by the amplified electronic signal. Secondly, the analog signal received by photodetector is collected and converted to digital signal. Thirdly, the digital signal is separated into n groups with the central wavelengths of $\lambda_1, \lambda_2 \ldots \lambda_n$, respectively, and then the data of n groups are synchronously processed in the FPGA with hardware Fast Fourier Transform (FFT). Through the integration of $\tilde{R}(v) = \int_{-\infty}^{\infty} R(v)\exp\left(-2\pi i\lambda v\right) d\lambda$, where λ is the wavelength, and $R(v)$ is FFT spectra with the peak frequency v of F_1, $F_2 \ldots F_m$, corresponding to different cavity lengths, the component of each frequency channels is filtered. Finally, the Inverse Fast Fourier Transform (IFFT), i.e., $R(\lambda) = (1/2\pi)\int_{-\infty}^{\infty}\tilde{R}(v)\exp\left(2\pi i\lambda v\right) dv$ (Zhang et al. 2012b), is performed for the m units simultaneously. As a result, all the sensor parameters

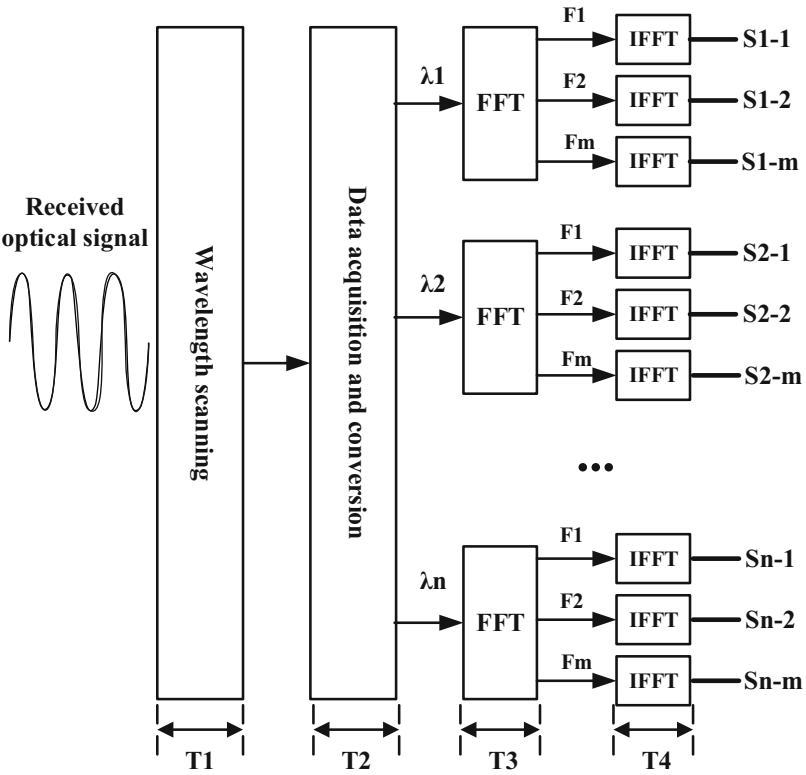

Fig. 12 Schematic of the parallel processing flow for the TDM/WDM microstructure sensor network. (Copyright 2019 IEEE)

can be recovered with high speed. According to this mechanism, a demodulation system with high wavelength resolution of 3 pm and high speed of 500 Hz in the C band was realized, demonstrating the possibility of quickly retrieving the sensing information for the TDM/WDM microstructure sensor network (Cheng et al. 2018).

Beneficial from the high spatial resolution and large capacity of the TDM/WDM microstructure sensor network , a high resolution manometry (HRM) was developed for measuring the pressure and motility of the gastrointestinal tract (Samo et al. 2016), by inserting the packaged sensing fiber into the gastrointestinal tract. Figure 13 illustrates the photographs of the HRM device with gastrointestinal tract pressure monitoring, packaged TDM/WDM microstructure sensing fiber with spatial resolution less than 1 cm, and the schematic of the HRM testing.

Because the bare fiber is only sensitive to the axial strain but almost insensitive to the lateral strain, pressure transducer is necessary for the sensing fiber to enhance the pressure sensitivity. As displayed in Fig. 14a, biocompatible silicon rubber

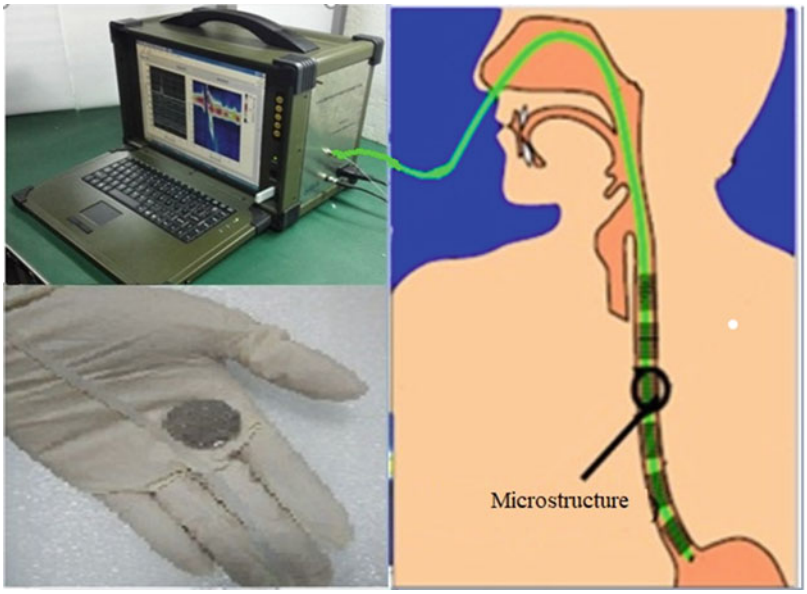

Fig. 13 HRM system based on TDM/WDM microstructure sensor network

was utilized to package the sensing fiber as a pressure transducer and protective coating. Regarding the linear deformation model of the silicon rubber under small pressure, the effective elastic modulus E_{eff} of the composite structure can be calculated as:

$$E_{\text{eff}} = \frac{A_f E_f + A_p E_p}{A_f + A_p} \tag{4}$$

where A_f, A_p are the cross-sectional area of the fiber and the polymer, and E_f, E_p are the elastic modulus of the fiber and the polymer, respectively. When the fiber was encapsulated in the center of the polymer with the diameter of 3 mm, the pressure sensitivity of the sensor was elevated to 2.22 nm/Mpa, which is much more sensitive than the bare FBGs sensor of 3 pm/Mpa. Further, the dynamic pressure response was investigated by tracking the pressure waves along the fiber. Figure 14b illustrates the experimental setup, where a 2 cm/s pressure wave was simulated by rolling a 100 g cylindrical metal stick over the packaged fiber, equivalent to the gastrointestinal tract pressure in vivo. The map of the real-time response is depicted in Fig. 14c, achieving the measurement of velocity, orientation, and value of the pressure wave, which provides information for the diagnosing clinician to find out the motility of the gastrointestinal tract clearly (Zhang et al. 2019 to be published).

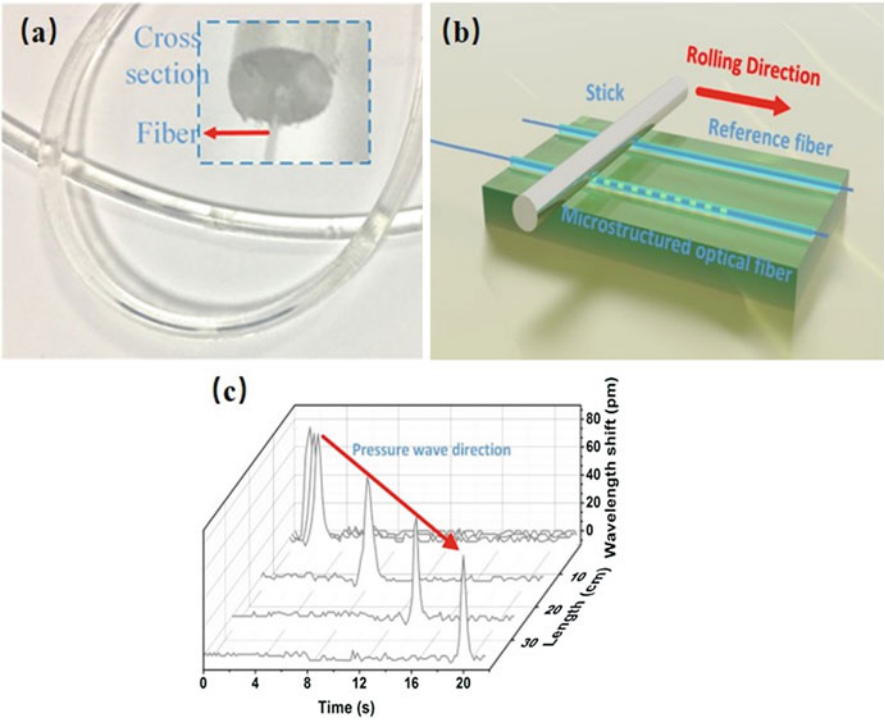

Fig. 14 (**a**) The photo of the packaged sensing fiber; (**b**) experimental set-up for pressure wave measurement; (**c**) the map of the real-time pressure response

Quasi-Distributed Sensor Network Based on 3D Encoded Microstructures

Based on the low-finesse FPI composed of two closely spaced UWFBGs, WDM/FDM/TDM quasi-distributed sensor network is further investigated to realize huge multiplexing capacity in a single fiber. On account of the FPI structure and weak reflectivity, the microstructure can be 3D encoded with different wavelength, frequency, and time slot, named as Wi, fj, and Tk, which are realized by choosing different central wavelengths λ_B of UWFBGs, different spatial distances between the UWFBGs pairs (defined as the cavity length L_C), and delay fiber with certain length.

The configuration of the WDM/FDM/TDM quasi-distributed sensor network is described in Fig. 15, including the microstructured optical fiber and the central office for demodulation. When a probe light pulse is launched into the sensing fiber, microstructures with same time code are first located and distinguished through the time delay of received pulses roughly. The demodulation module analyzing the spectrum to obtain the wavelength and frequency information can be used to locate every single microstructure. Owing to this 3D encoding mechanisms,

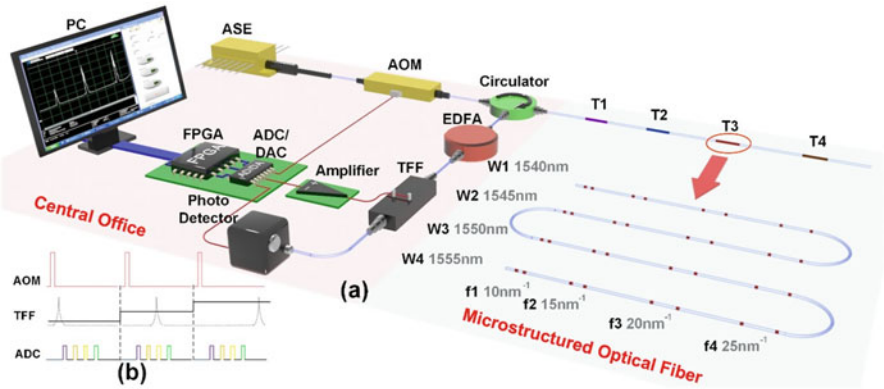

Fig. 15 Configuration of the WDM/FDM/TDM quasi-distributed sensor network: (**a**) experimental setup; (**b**) driving signals of AOM, TFF, and ADC in M-OTDR. (Copyright 2019 Springer)

microstructures spaced closely to each other can be further separated through wavelength and frequency encoding within one time domain, overcoming the restriction of spatial resolution in TDM scheme. The multiplexing capacity could reach to 18,000 when the reflectivity of the UWFBG is as lower as −40 dB (Sun et al. 2017). It can be seen that the quasi-distributed sensor network based on 3D encoded microstructures is able to provide enough sensing points and very flexible configuration for different kind of sensing applications.

As shown in Fig. 15a, the demodulation scheme is based on a tunable FP filter (TFF) and 3D decode through spectrum analysis. The probe light from Amplified spontaneous Emission (ASE) source is modulated into pulses by the acoustic optical modulator (AOM). The modulated light pulses are directed into the sensing fiber. The back-scattered pulses carried with sensing parameters are amplified by an erbium-doped optical fiber amplifier (EDFA) and filtered by the TFF. Avalanche photo detector (APD) transfers the optical signals into electrical ones. The DAC&ADC module (composed of an NI 5781 adapter module and an NI 7962 FPGA module) synchronously controls the modulate time of the AOM and the TFF through DAC, as well as the sequential logic of electrical data captured by ADC. The driving voltage of AOM is a series of voltage pulses with the width of 200 ns, while that of the TFF is modulated in a sawtooth wave (Wang et al. 2018a). It should be noted that scanning nonlinearity and temperature sensitivity of the TFF will seriously affect the demodulation accuracy and stability.

To resolve this issue, an improved demodulation scheme with self-calibration to actively compensate the error induced by TFF was proposed, as illustrated in Fig. 16a. A wavelength calibration unit with multiple reference FBGs is utilized with 3-order polynomial fitting to auto-calibrate the real-time relationship of TFF, and thus to eliminate the demodulation error. Note that the reference FBGs, which can be replaced with any optical filter device, are placed in an incubator chamber to keep the wavelengths constant. Pre-scanning and Polynomial fitting of the TFF function

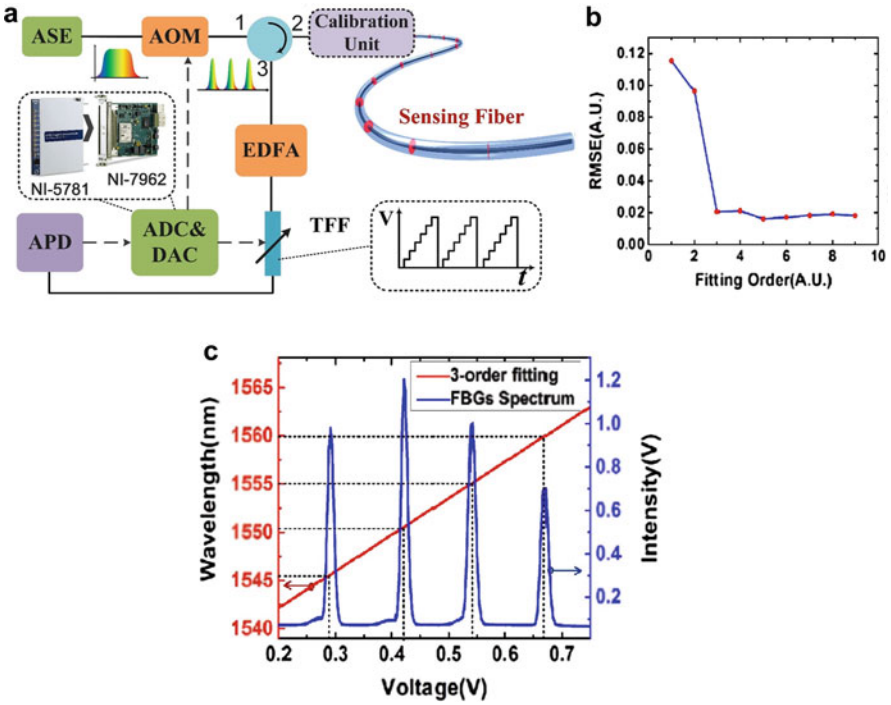

Fig. 16 Schematics of the demodulation platform with self-calibration: (**a**) system configuration; (**b**) the RMSE at different Polynomial fitting orders from 1 to 9; (**c**) spectrum of reference FBG s and the fitting curve. (Copyright 2019 IEEE)

is carried out by launching the tunable laser. Fittings with different fitting orders are established, and the root-mean-square errors (RMSE) are depicted in Fig. 16b, which indicates that linear fitting will induce greater demodulation error and 3-order polynomial fitting is enough for the demodulation. The detected spectrum of FBGs at a random moment and its real-time fitting curve are depicted in Fig. 16c, compensating the demodulation deviation (Wang et al. 2018a). The experimental results demonstrated that the demodulated wavelength deviation was only 6 pm when the temperature of TFF changes for 9.3°C, the wavelength demodulation resolution was 1 pm, and the long-term demodulation precision was 3 pm, which could provide reliable measurements in large engineering projects.

Special Fiber Grating Sensor Network and Applications

In comparison with ultraviolet (UV) lasers, femtosecond lasers may be a more powerful and versatile inscription source and have opened up a new territory for grating and microstructured fiber devices. Apart from seeing many successful commercial deployments of fiber grating sensors, novel and function-enhanced

grating-based sensor structures have been developed for unique and high function sensors, by utilizing specially modified or tailored grating structures and special fibers. The exploitation of special grating structures and fibers and the combination with micro-nano features have broadened the sensor technology field for novel and high function optical fiber sensors. In the following, several special fiber grating sensors for network and their applications will be studied.

Tilted Fiber Grating (TFG) Sensor Network and Applications for near Infrared Detection (NID)

In some applications, such as food safety, petrochemical process control, and pharmaceutical production quality control and agriculture area, the indirect detection method was not suitable any longer. So far, the main detection method used in those areas was analytical chemistry technique, which included near infrared spectroscopy, gas/fluid chromatography, nuclear magnetic resonance etc. Among them, near infrared (NIR) technology owns many advantages such as rapid process, nondestructive, noninvasive, chemical free, universal application, and suitable for process analytical technology and quality control (Woodcock et al. 2008; Jamrógiewicz 2012; Cleve et al. 2000).

In NIR detection field, silica optical fiber has been employed as light energy transmitting optical fiber for application in harsh environment, owing to its low transmission loss at the NIR bandwidth. However, it has always been the focus of scientific research and exploration how to use the fiber to realize the distributed multi-point NID. There are several techniques to lead light transmitted inside the fiber core to out of fiber, including side-polished fiber, taped fiber, and fiber grating. Using side-polished fiber and taped fiber, light could interact with analyte by evanescence wave, which has very limited detection depth. The radiation of fiber grating offers a power controllable and effective method to achieve the analyte detection. Specifically, the 45° TFG is the most effective radiation fiber grating, by which the light transmitting inside the fiber core could be partially coupled out. Figure 17a presents the working principle of the 45°-TFG based on Brewster law, in which the light of transverse electric (TE) polarization is coupled out of fiber core and into radiation modes, and the light of transverse magnetic (TM) polarization still transmits inside the fiber core. Hence, the 45°-TFG can be treated as an ideal in-fiber power taping device. According to the previous analysis (Yan et al. 2011, 2013), the taping ratio of TE polarization depends on UV-induced index modulation and the length of grating, which are easily adjusted by controlling the exposing time and grating length. Figure 17b shows the simulated results of taping ratio with different index modulations and grating lengths at the wavelength of 1500 nm.

The most organic molecules have their fundamental characteristic absorption band at infrared area; their combine band would be located at the NIR area. In the mathematic, the light propagation in absorbing materials can be described using a complex valued refractive index. The real part of the refractive index indicates the phase velocity, while the imaginary part indicates the amount of absorption

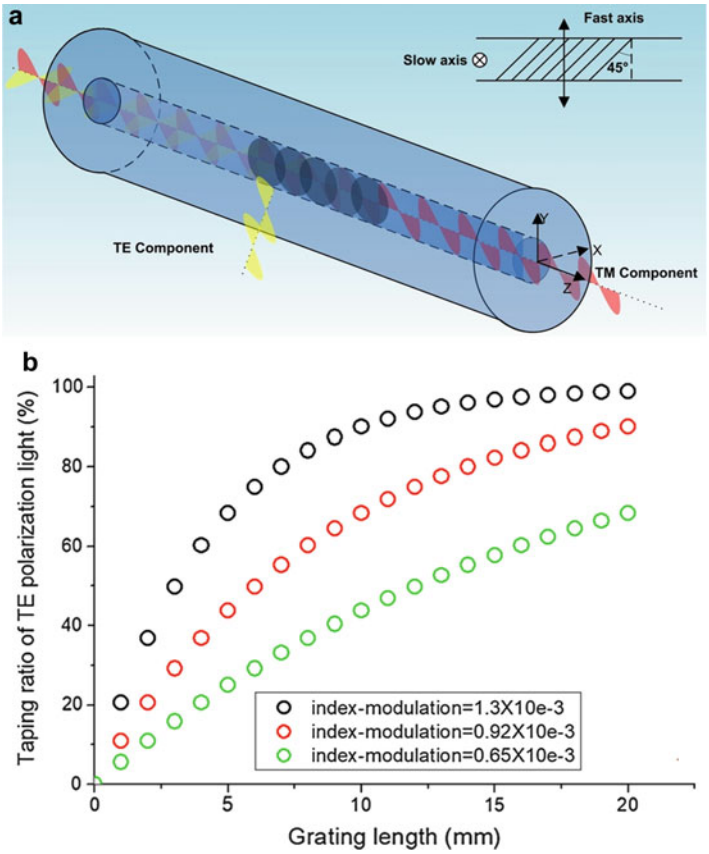

Fig. 17 (**a**) The structure diagram of 45°-TFG; (**b**) taping ratio of TE polarization of 45°-TFG with different grating lengths

loss when the electromagnetic wave propagates through the material. In terms of the absorption mechanism, the 45°-TFGs-based NIR detecting system consisting of 45°-TFGs, low-cost photodetectors, and single-wavelength laser diodes would be potentially used for distributed NIR detecting system. As shown in Fig. 18, the developed prototype 45°-TFG NIR detection system is an optical fiber transmission system, which can be used for multi-point detection. Each detection unit contains one major probe grating and one reference grating. During the measuring process, the light coupled from the reference 45°-TFG is directly reflected to the detector without any interaction with sample. While the light coupled from the probing 45°-TFG is launched to the surface of sample, the reflected/scattered light signal will give information on the probe content due to absorption.

A range of flour samples with different moisture levels were subjected to the measurement under this system. The different moisture level flour samples were prepared by leaving the fully dried (0% moisture level) flour sample in the air for

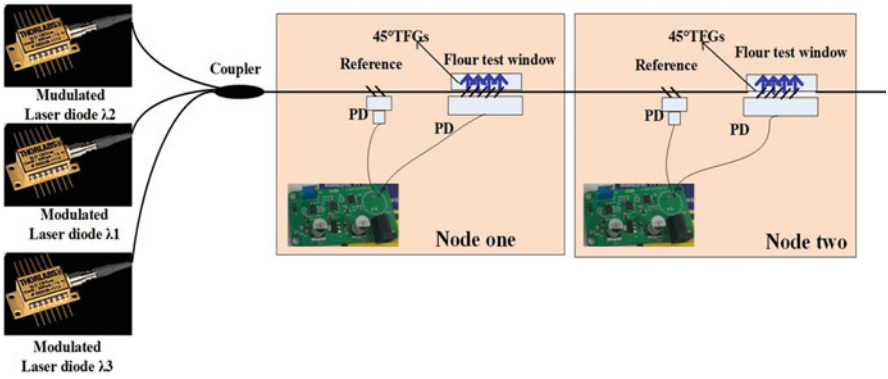

Fig. 18 Configuration of 45°-TFG-based distributed NIR detecting system

a period, then by weighting the mass increment of sample, the moisture level of flour sample was calculated. Fully dried flour sample was prepared by keeping the flour sample at 80 °C oven for 24 h. To make sure the testing flour sample has uniform density and maintains at certain moisture level, in the experiment, 1g weight dried flour sample was filled into small container and left in air to absorb water and then sealed into a small container. Figure 19a shows NIR absorption spectra of flour sample with 10% moisture and 11.4% protein content measured from 1260 to 1580 nm, indicating a similar shape with the one shown in the reported research (Manley 2014). The flour samples were also tested with different moisture levels from 0% to 15.6% at 1450 nm (see in Fig. 19b). The result shows Log(1/R) ($R = \frac{I_{\text{reflectance}}}{a \times I_{\text{reference}}}$, where $I_{\text{reflectance}}$ is the signal intensity reflected from the surface of sample; $I_{\text{reference}}$ is the signal intensity of reference light; a is the correction factor.) is linearly proportion to the moisture level with high sensitivity around 0.014/% and low mean square error around 0.977.

Figure 20 displays the first 45°-TFG-based NIR detection prototype system, which has been installed in the UK Warburtons baking production line for flour moisture test. The benefits of this 45°-TFGs-based NIR detecting system are low loss, compact structure, collimation free, and suitable for long distance, distributed operation. In future, the NIR system would be optimized to compensate the measuring error caused by physical property of sample, such as particle size, and achieve multicomponent measurement.

Er^{3+} Doped Fiber Grating Sensor Network and Applications

Compared to the passive Bragg gratings, fiber grating lasers, which are realized by inscribing gratings in Er^{3+} doped fiber (EDF), not only possess a higher SNR but also offer a large-scale multiplexing capability. Actually, the fiber grating laser sensors mainly adopt the distributed feedback fiber laser (DFBFL) and the

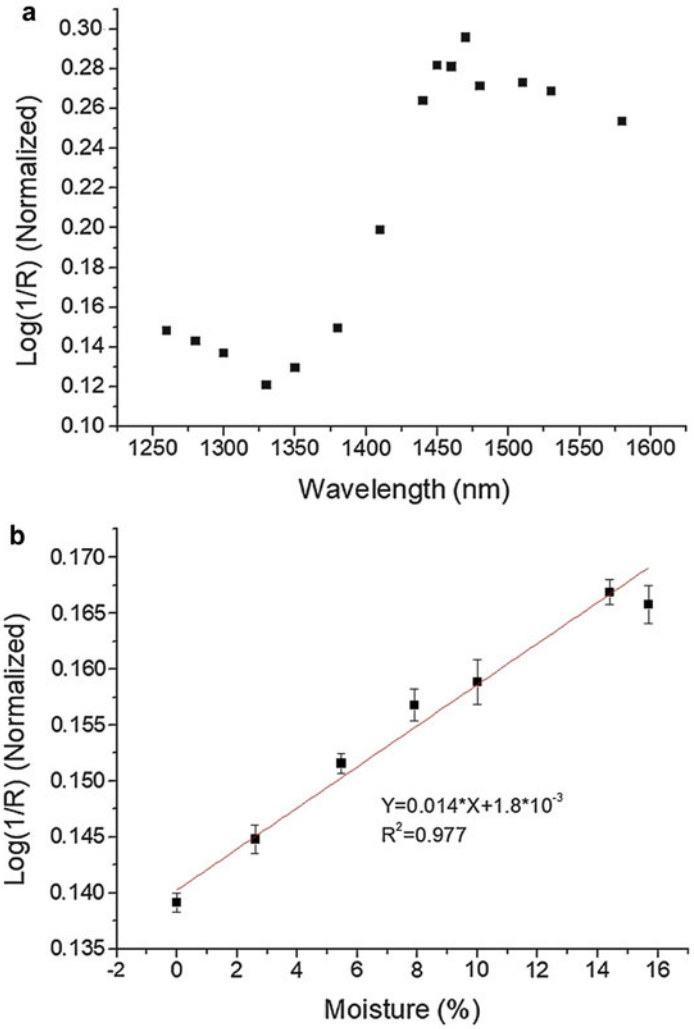

Fig. 19 (**a**) The NIR absorption spectra of flour sample with 10% moisture level and 11.4 protein content; (**b**) the measurement for flour sample with different moisture level at 1450 nm

distributed Bragg reflector fiber laser (DBRFL) as the sensing elements, which can be categorized into wavelength encode sensor and polarizer encode sensor with respect to their detection mechanism. Specifically, the DBRFL operates in single longitude mode with two orthogonal polarization modes and converts the measurand into change in the polarization modes beat frequency. Thanks to the advantages of easy interrogation, high measurement resolution, absolute encoding, and so on, the DBRFL sensors have attracted considerable interest in recent years.

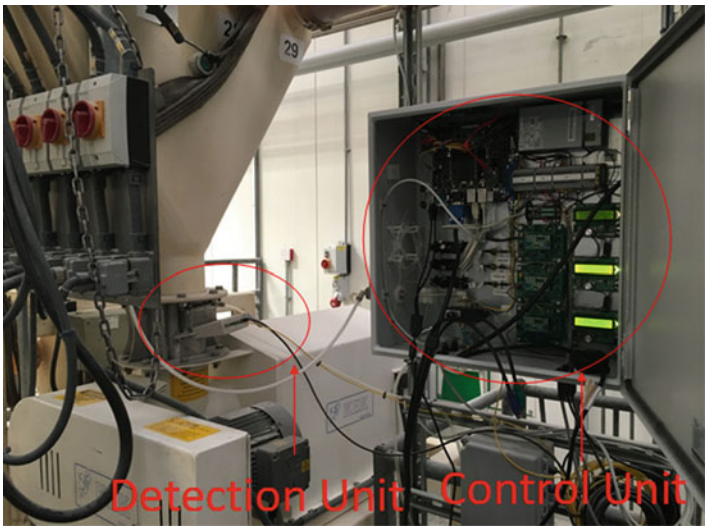

Fig. 20 Flour moisture detection through a compact 45°-TFG-based distributed NIR detecting system

As illustrated in Fig. 21a, the DBRFL sensor is composed of two wavelengths matched Bragg gratings pair written in a short length of EDF directly. Due to the fiber birefringence, the laser always operates in two orthogonal polarization states, and when the laser output is monitored by a photodetector (PD), the two polarization modes will generate a beat signal in the radio frequency domain (Wo et al. 2012). The beat frequency is given as (Guo et al. 2011):

$$\Delta\nu = Bc/n_{\text{eff}}\lambda_0 \tag{5}$$

where c is the light speed in vacuum, λ_0 is the laser wavelength, n_{eff} and B are the average refractive index and birefringence of the optical fiber, respectively. By carefully optimizing the cavity parameters such as the absorption of EDF, reflectivity, Bragg wavelength and bandwidth of the gratings, single-frequency lasing can be easily achieved when the cavity length reduces to several centimeters (see Fig. 21b). Meanwhile, very low noise floor of the beat signal can be achieved, where the noise power spectral density exhibits a C/f profile with the factor C about 3.923×10^4 (Hz^2) (as shown in Fig. 21c). When an external measurand is applied on the laser cavity, the fiber birefringence will change linearly due to the elasto-optic effect, as well as the beat frequency of the two polarization modes.

Similarly to the passive FBG sensors, the DBRFL sensors can be multiplexed in a single fiber through WDM and FDM . A sensor array consisting of as many as 16 DBRFLs have been presented, which were wavelength multiplexed by inscribing fiber gratings with different pitches, and frequency multiplexed in RF domain by controlling the intracavity birefringence. The lasing wavelengths range from 1528.8

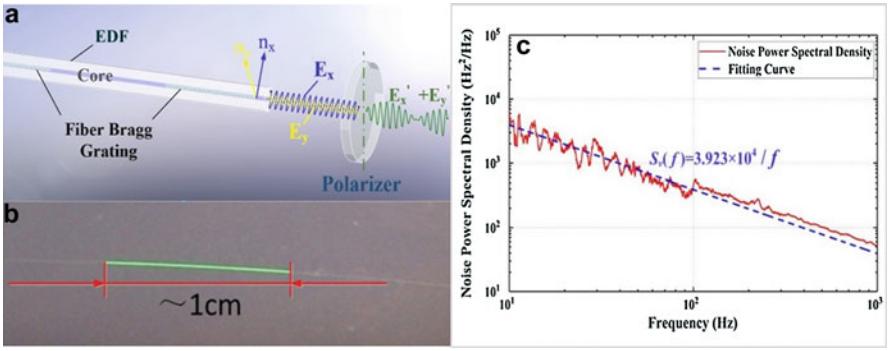

Fig. 21 Schematic diagram of DBRFL: (**a**) structure and principle of DBRFL; (**b**) photo of the short cavity DBRFL; (**c**) frequency noise power spectral density of the DBRFL

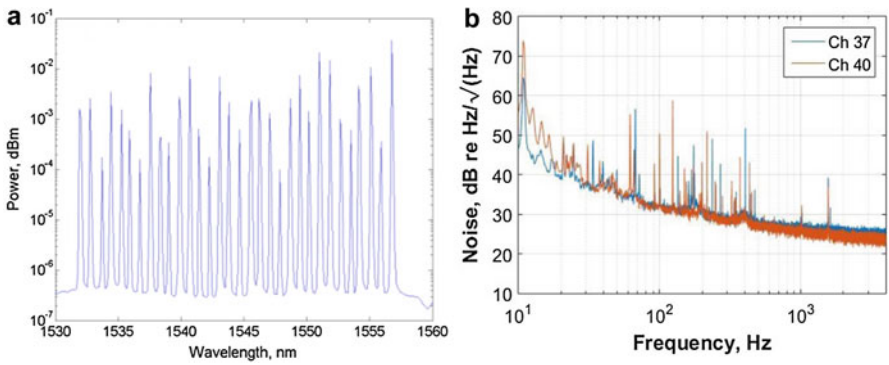

Fig. 22 The optical spectrum (**a**) and frequency noise spectra (**b**) of the multiplexed DBRFL sensor network. (Copyright 2019 OSA)

to 1566.4 nm with the spacing of 2.4 nm and SNR higher than 35 dB, and the output beat frequencies ranges from 140 MHz to 1.7 GHz, controlled by the CO_2 laser side irradiation to the laser cavity (Jin et al. 2014). Besides, through specially design the DBRFLs to eliminate out of band reflections (minimize laser-laser interactions), decrease the laser pump threshold (~1 mW at 1480 nm) and energy absorption per device (<0.4 dB), 32 DBRFL sensors were successfully wavelength multiplexed on a single fiber with output wavelengths matched to channels 26–57 of the C-band 100 GHz ITU grid (Harrison and Foster 2017). The optical spectrum of the multiplexed fiber laser array is shown in Fig. 22a, and Fig. 22b presents the frequency noise spectra of different DBRFLs. Certainly, the DBRFL is a credible candidate for large capacity sensing network.

The DBRFL sensor network has been successfully demonstrated for measuring different parameters, such as lateral force, vibration, acceleration, displacement, bending, ultrasound, current, etc. One typical application is developed for pulse and respiration monitoring for body health (Sun et al. 2014). As depicted in Fig. 23a,

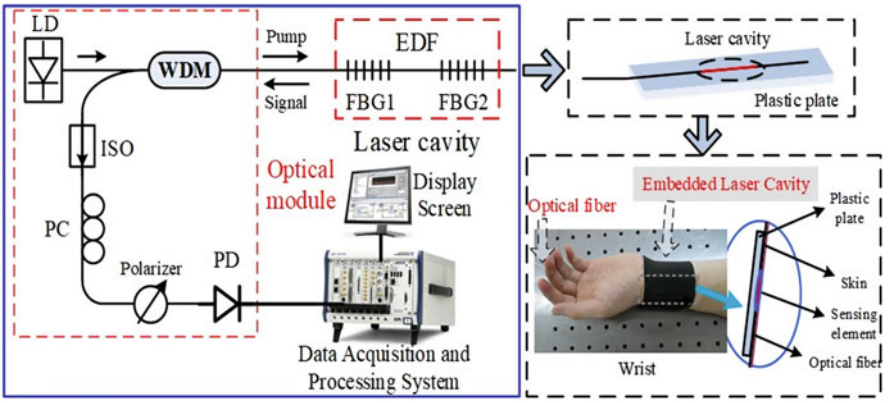

Fig. 23 The schematic diagrams of: (**a**) DBRFL based sensor system; (**b**) the packaged sensing device for pulse monitoring; (**c**) the assembling and fixing method for the wrist pulse monitoring. (Copyright 2019 SPIE)

the laser cavity with the physical length of only 10 mm is selected as the sensing element. A 980 nm laser diode is launched to illuminate the laser cavity through a 980/1550 nm WDM. The backward lasing output is injected into a data acquisition and real-time processing system (NI PXIe-1082) through a PD via an isolator (ISO), a polarization controller (PC), and fiber polarizer. By adjusting the PC, the beating signal intensity of the two orthogonal polarization modes could be maximized. The beat frequency signal received by the data process system is then acquired and displayed using the application program based on LabVIEW platform. To fabricate the transducer for arterial pulse monitoring, the laser cavity is first attached onto an elastic and flexible plastic plate with epoxy adhesive, and then tightly fixed onto the arterial pulse position (for example wrist artery) of a person with the help of textile belt, as displayed in Fig. 23b, c. The detail in Fig. 23c presents how the plastic plate is attached onto the wrist pulse. The fiber is kept straight during the packaging process to eliminate any bending effects.

As illustrated in Fig. 24a, the beat signal changes with time periodically and the maximum frequency change is about 10 MHz. In this arterial pulse waveform, the sharp rising edge indicates a contraction behavior of the artery, while the slow falling edge represents the artery relaxation behavior. Also, the incisura of the dicrotic notch to the end of diastole of the artery pulse wave is clearly depicted in Fig. 24b, which is accordant with the practical situation. Actually, the dicrotic notch is a very important and meaningful characteristic parameter for the cardiovascular disease diagnosis. From the pulse waveform, pulse rate could also be obtained. Each time when the beat signal reaches the systolic peak, the pulse beat count is incremented once. The investigation results in Fig. 24c indicate that the average pulse rate of the sample is around 75 times per minute.

Further, by using a 10×27 mm^2 solid plastic plate to support another laser cavity, the DBRFL sensor network can be simultaneously employed for monitoring

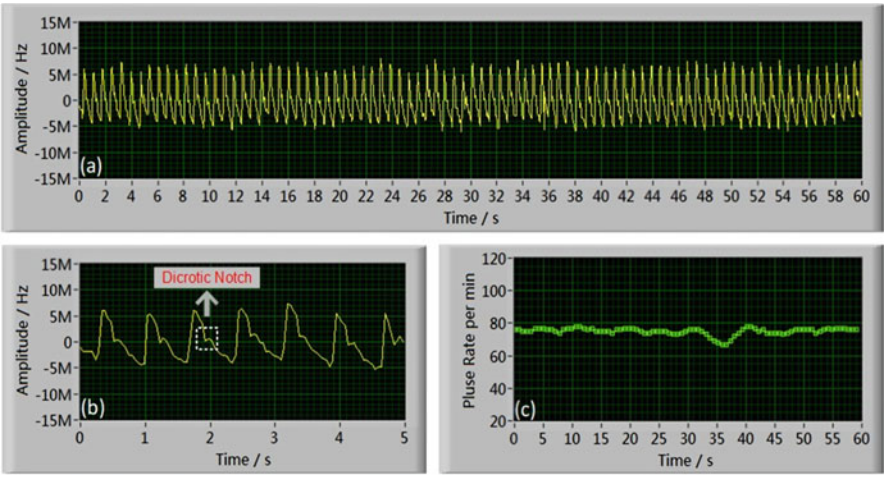

Fig. 24 Recorded wrist arterial pulse for tested person: (**a**) waveform within 1 min; (**b**) enlarged 5-s fragment from (**a**); (**c**) calculated average pulse rate during 1-min recording. (Copyright 2019 SPIE)

respiration activity (Wo et al. 2014), as shown in Fig. 25a. The textile belt is fastened tight on the abdomen position of the tested person, and then the respiration movement including both the contraction and relaxation behavior will lead the elongation of the flexible textile, which change the transverse pressure applied onto the laser cavity. In this case, the respiration strength, as well as the breath rate could be obtained simply by monitoring the frequency change of the beat signal.

Figure 25b, d give the recorded the respiration waveforms for the two persons within 1 min when the DBRFL sensor is subjected to the elongation of the abdominal circumference during respiration movements. It can be seen that the beat signal changes with time periodically and the maximum frequency change is about 8 MHz for subject A and 4 MHz for subject B, and the inhalation and exhalation behavior of the respiration can be clearly observed. In addition, the respiration rate can be obtained through Fourier transformation of the respiration waveform. Figure 25c, e indicate that the breath rates of the two persons are 12.60 and 19.32 times per minutes, respectively. The excellent performance of the DBRFL sensor network paves a new way for monitoring multiple healthy parameters.

Fiber Optic Sensors Passive Optical Network (SPON) and Applications

Most of us are familiar with the topology of FTTX, which consists of the optical line terminal (OLT), the passive optical network, and the active optical network units (ONU). The downstream is broadcasted from OLT to every ONUs, while the upstream is directionally transmitted from certain ONU to OLT. According to

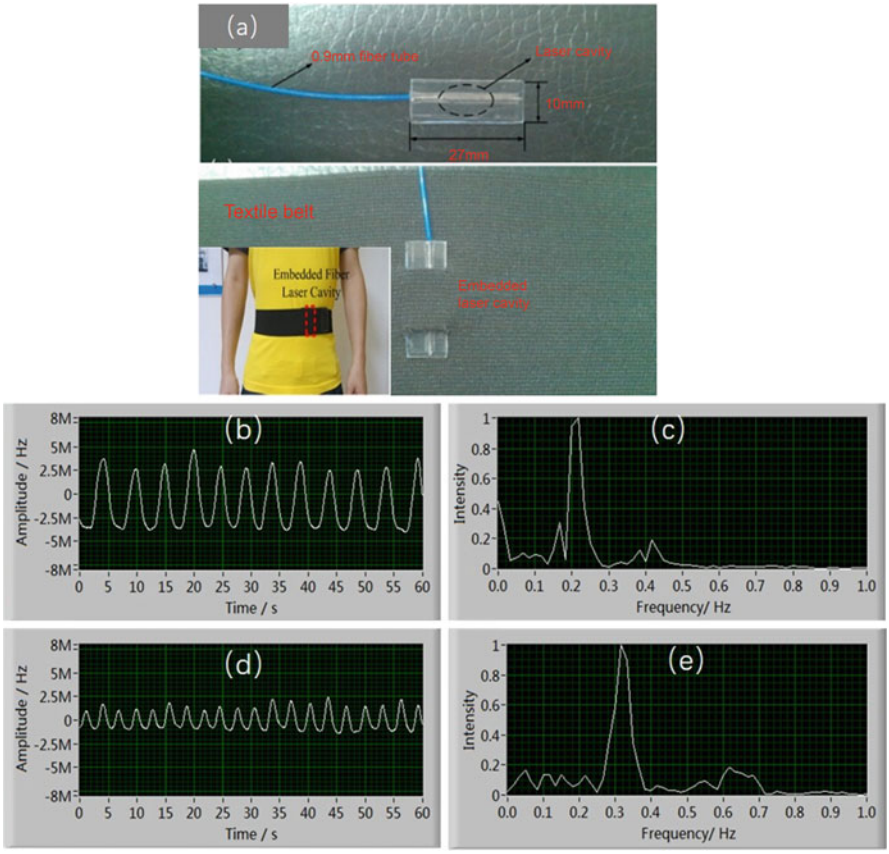

Fig. 25 (**a**) Fixture of the laser cavity for respiration monitoring; recorded respiration waveform for subject A (**b**); and subject B (**d**); frequency spectrum of respiration waveform for subject A (**c**); and subject B (**e**). (Copyright 2019 SPIE)

this configuration, the similar architecture for fiber sensor network, named as fiber optic sensors passive optical network (SPON), was proposed (Liu et al. 2016). As represented in Fig. 26, the SPON is also composed of three main parts, OLT, ODN, and optic sensor units (OSU). However, it is different with the communication PON. Firstly, the transmission data from OLT is always analog, and is broadcasted to every OSU from ODN. Secondly, the OSN is always passive due to the characteristics of optical sensor. Hence, in order to make the SPON work effectively, the OSU should be of self-feedback, that is, it can reflect the modulated signal which carries the sensing information to the OLT through the ODN, and then the modulated signal can be demodulated at OLT to achieve the sensing parameters. In this network architecture, the OSU can be multi-functions, multi-structures, and multi-points, as long as the OLT can provide appropriate light source, as well as signal demodulation processing. And the OSUs can be multiplexed through WDM, TDM, FDM, and

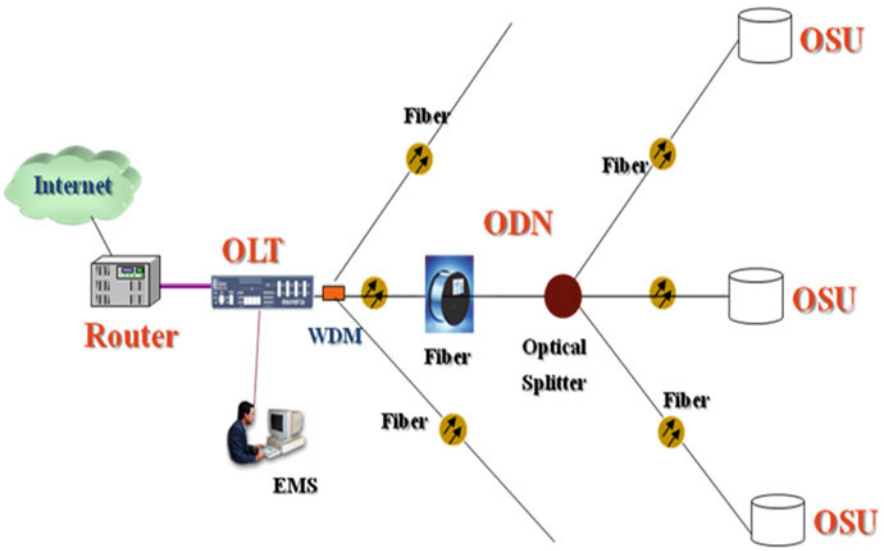

Fig. 26 Schematic diagram of the architecture of SPON. (Copyright 2019 Springer)

their combinations. Therefore, the SPON is of large capacity, good adaptability, high extendibility, and great flexibility as the communication PON. Next, several types of SPON architectures including the star topology and tree topology networks, and their practical applications will be presented.

TDM-Based Fiber Optic Acoustic SPON

Acoustic sensors have been widely used in scientific research and industrial applications, such as the study of vector sound field, acoustic imaging, underwater detecting, nondestructive testing (NDT) for large structures, partial discharge (PD) detection in power transformers, and photoacoustic gas detection. In addition to high sensitivity, the real-time multipoint measurement is also a common demand in the above applications. Acoustic sensor array can map the distribution of the whole sound field, thus to better locate and identify the characteristic events. Optical fiber acoustic sensors have unique advantages of multiplexing, high sensitivity and excellent immunity to EMI. In this part, a diaphragm-based optical fiber acoustic sensor array with the help of TDM and coherent phase detection will be reported. A prototype sensor array was developed and successfully applied in several fields.

The system configuration of the fiber acoustic SPON is illustrated schematically in Fig. 27a. Multiple sensor tips are connected by a 1*N coupler with single mode fiber (SMF) delay line (DL) in different length, and multiplexed through TDM, constructing a star topology network. Figure 27b depicts the structure of one

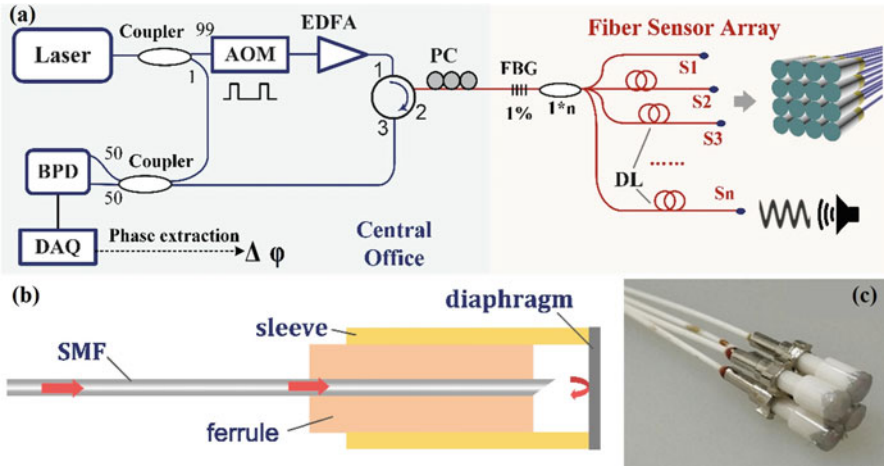

Fig. 27 (**a**) Schematic of multi-point acoustic sensing system using coherent detection. (**b**) Schematic of the sensor tip; (**c**) photograph of 2 × 2 sensors array. (Copyright 2019 OSA)

acoustic OSU in detail. A ceramic sleeve with the side opening is tightly assembled to a ceramic ferrule, in which an optical fiber pigtail is fixed central. The facet of fiber pigtail is polished with an angle of 8° to reduce the Fresnel reflection from the fiber end. A 10-layer graphene diaphragm is smoothly glued on the top of the sleeve with UV-curable adhesive. The extremely thin graphene diaphragm is covered with PMMA, with the total thickness of about 5 nm. The sensor tip is about 2.5 mm in diameter, while the distance between graphene diaphragm and fiber facet is several hundred micrometers (see the photograph of sensor tips in Fig. 27c). When the acoustic wave is applied on the sensor tip, the diaphragm vibrates accordingly, resulting in the length change between the diaphragm and fiber facet. In this way, the optical phase modulation of the reflected light from the diaphragm is achieved (Wang et al. 2018b).

As the reflection signal from graphene diaphragm is weak, coherent phase detection technique for improving the signal-to-noise ratio (SNR) is employed for the sensor array, which up-converts the acoustic signal into the high sideband frequency to reduce the noise. Hence, the laser with narrow linewidth outputs continuous light of 1550 nm, which is split into the probe light and the local-oscillator light by 99:1. The probe light is modulated into pulses with the width of 10 ns through an acoustical optical modulator (AOM), as well as being frequency shifted by 200 MHz. After amplified by an EDFA, the probe light pulses launch into the sensing fiber through a circulator. The injected pulses are partly reflected by a FBG before entering into the sensor array. Note that the weak FBG here serves as the referenced reflection point with fixed optical phase. The reflected pulses from sensor array are carried with acoustic signals and interfere with the local-oscillator light. The generated beat frequency signals are received by a balanced photo detector (BPD) and collected by a data acquisition card (DAQ module from National

Instrument with sample rate of 2 GS/s). Due to the different time delay of reflected pulses, beat frequency signals from different sensor tips can be distinguished in time domain (Wang et al. 2018b).

For *TDM*-PON, the capacity is mainly determined by the power budget, and the theoretical capacity N can be deduced as follow:

$$N \leq \sqrt{\frac{r\,(1-R)}{5\Delta L \alpha_R S_{\mathrm{n}}}} \tag{6}$$

Where R and r are the reflectivity of the weak *FBG* and graphene diaphragm, respectively; ΔL is the length of injected light pulse; α_R and S_n represent the Rayleigh scattering coefficient and the ratio of backscattered Rayleigh scattering, which is about 0.032×10^{-3}/m and 10^{-3}, respectively in SMF. Assuming that $R = 1\%$ and $r = 2\%$, the maximum network capacity will reach to 248 and can be further increased by using a sensing diaphragm with higher reflectivity (Wang et al. 2018b).

The sensing performances were experimentally investigated and presented in Fig. 28. The result in Fig. 28a exhibits relative high sensitivity of larger than −136 dB re 1 rad/μPa within the full measured frequency range from 300 Hz to 15 kHz. And a resonance peak appears at 1.2 kHz with the sensitivity up to −119 dB re 1 rad/μPa. As seen from Fig. 28b, the SNR is about 37.68 dB, corresponding to the MDP of only 75 μPa/Hz$^{1/2}$. The fluctuation of the output signal is about 0.66 dB (see Fig. 28c), proving high measurement stability under the large variation of temperature. In addition, the curves of different frequencies in Fig. 28d exhibit excellent and flat acoustic response with wide directivity, where the normalized acoustic sensitivity is optimal at 0° and only decreases to 0.72(−2.85 dB) within the angle range of ±90°. Although the frequency response of the sensor is not flat and broadband, it can be optimized by specially designing the diaphragm. The excellent MDP, high temperature stability, wide directivity, and large multiplexing capacity make the acoustic SPON favorable for acoustic detections in industrial applications (Wang et al. 2018b).

The fiber acoustic SPON can realize multipoint acoustic detection, providing the typical application for sound source localization. Three sensor tips can form the smallest sensor array system for two-dimensional (2D) sound source localization. As shown in the Fig. 29a, b, three sensors are placed at the three vertices of a square. A point acoustic source is set in the square and emits the sound wave at one specific moment, then the sound waves propagate through medium and detected by the sensor array simultaneously. Then the waveforms measured by three sensor tips have similar morphological characteristics but different in timing. While the time difference of arrival (TDOA) can help to calculate the distance difference $\triangle x_{ij}$ of every two sensors to the sound source, hyperbolic positioning algorithm is adopted to locate the sound (Fu et al. 2014). The intersection of the two solid hyperbola lines corresponding to $\triangle x_{23}$ and $\triangle x_{13}$ is the location of the sound source. Through this way, the coordinate is calculated to be A′, which is very close to the actual

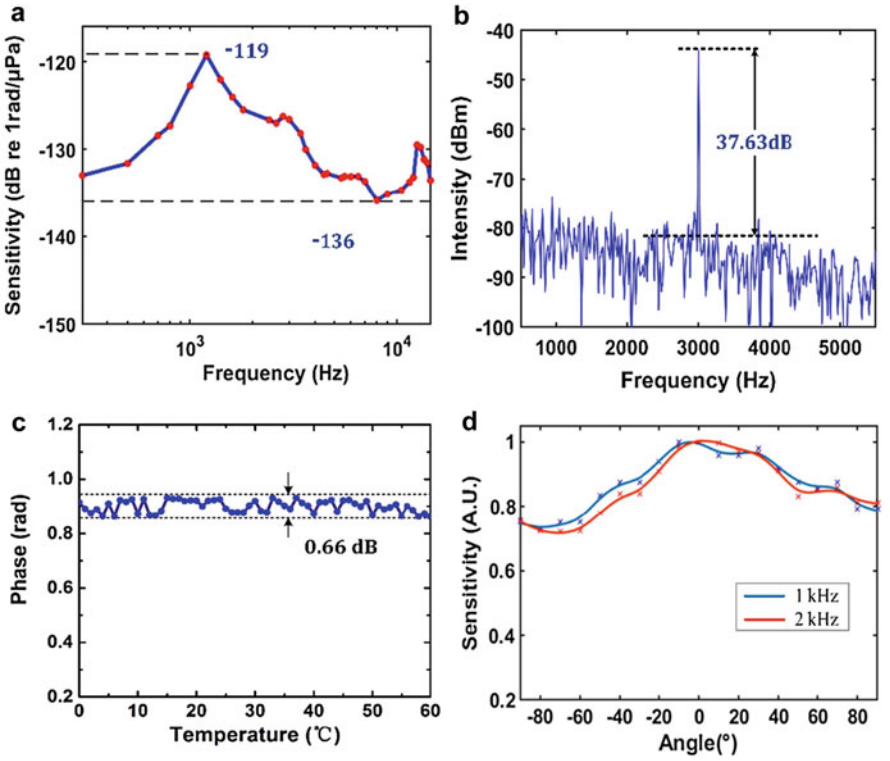

Fig. 28 Sensing performances of the sensor tip: (**a**) Frequency response from 300 Hz to 15 kHz; (**b**) Power spectrum of the measured signals when an acoustic pressure level of 25.7 mPa at 3 kHz was applied. (**c**) Temperature stability from 0 to 60 °C; (**d**) Normalized sensitivity with different acoustic incident angle. (Copyright 2019 OSA)

position A. The multiple tested results in Fig. 29c demonstrates that the maximum positioning deviation is 3.55 cm, which can be further improved by increasing the sampling rate, and the number of sensor tips.

Fiber optic hydrophone is the key device in the applications of underwater detection (Vidakovic et al. 2016; Kim et al. 2017). In the light of the above sensing principle and networking mechanism, a polymer diaphragm-based fiber optic hydrophone was developed, with a metal sleeve to resist the hydrostatic pressure and a 20 μm thickness PDMS diaphragm as the sensing part (see Fig. 30a). This sensor tip can meet the demands of high SNR, low frequency, and large multiplexing capacity to suppress the ocean noise. To calibrate the hydrophone in low frequency, a calibrator based on a vibrating column of liquid was built. As shown in Fig. 30b, d, the calibrator consists of a vibration exciter at the bottom and a half meter height tank, which uses an open column of liquid so that the wavelength of acoustic wave can be larger than the length of the column for low frequency detection. As seen from Fig. 30c, the undertest hydrophone and the

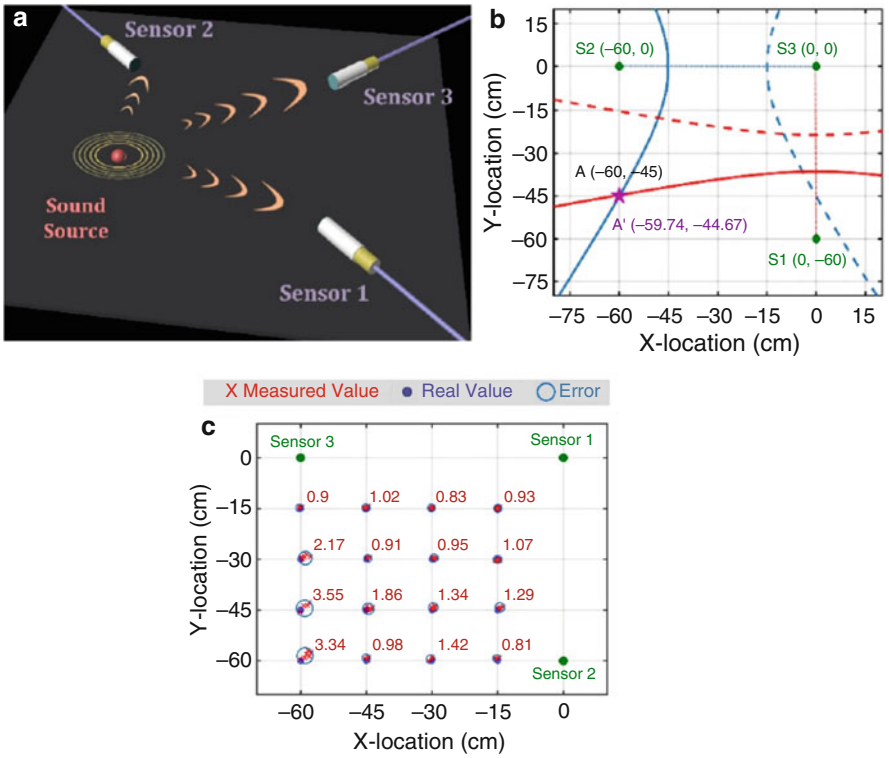

Fig. 29 Application for sound source localization: (**a**) schematic diagram of the working principle; (**b**) result of sound source localization with hyperbolic positioning technique; (**c**) positioning error assessment of sound source localization. (Copyright 2019 OSA)

reference hydrophone are placed at a same depth in the tank to achieve the reliable calibration.

The sensing performance of the polymer diaphragm-based fiber optic hydrophone was evaluated. From Fig. 31a, b, it can be seen that the fiber hydrophone could recover the acoustic signal with high fidelity and high SNR of 60 dB. As shown in Fig. 31c, the sensitivity of the air acoustic signal is as high as −120 dB re 1 rad/μPa with a flat frequency response from 50 to 800 Hz, while the sensitivity of the underwater acoustic signal is about −135 dB from 50 to 500 Hz with the non-uniformity less than 2 dB, which corresponds to the MDP of 300 μPa. Notably, the degradation of the sensitivity and resonant frequency underwater are mainly ascribed to the flow resistance of the water. Also, the response of the hydrophone in water at 100 Hz is plotted in Fig. 31d, where the underwater acoustic response is linear along with the pressure below 180 Pa, corresponding to a large dynamic range up to 118 dB.

Moreover, the fiber acoustic SPON can be used for pulse wave monitoring and diagnosis, which is an important tool in Traditional Chinese Medicine (TCM)

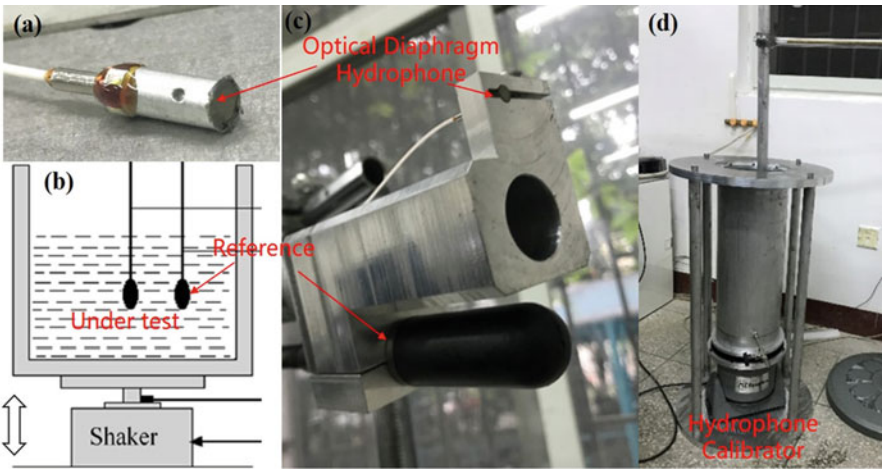

Fig. 30 (**a**) Photograph of the polymer diaphragm based hydrophone; (**b**) schematic of the calibration platform for low frequency underwater acoustic detection; (**c**) photograph of the diaphragm based hydrophone and the referenced hydrophone installation; (**d**) photograph of the calibration equipment

(McVeigh et al. 1999). As illustrated in Fig. 32a, b, the sensor tip is made of an aluminum diaphragm with 12 μm in thickness and a fiber pigtail with about 1 cm in diameter, to provide high-precision pulse wave monitoring. Wrist radial artery is chosen as measurement site and the fiber sensor tip is embedded into a sports-wristband to form a wearable device. The radial artery is usually chosen as the pulse monitoring location because the support of the radius facilitates the fixation of contact pulse sensor. Heart pumps blood and generates pressure signals in the artery which is detected by noninvasive fiber sensors as described in Fig. 32c, reflecting in the regular expansion of blood vessel walls.

A typical pulse waveform is plotted in Fig. 33a. Generally, the pulse cycle is divided into systolic phase and diastolic phase, the junction of which is called the dicrotic notch. In systolic phase, the blood is pumping from heart, resulting in a sharp rise in blood pressure which corresponds to the main wave in pulse waveform. And the predicrotic wave is formed by the multiple reflections of arterial wall. In diastolic phase, the aortic valve closes. The elasticity of the vessels causes a small amount of blood pumping back to the heart, creating a brief rise in blood pressure, appearing as dicrotic wave. From the pulse waveform, the widely used assessment indicators including augmentation index (AIx), average blood pressure(Pm), systolic blood *pressure* (SBP), diastolic blood pressure (DBP), blood viscosity (V), and the morphological description index of pulse waveform(K) can be calculated according to the formula in Fig. 33a (Avolio et al. 2009).

The pulse waveforms of four subjects aged between 22 and 24 years old were measured by the developed system, of which the details were restored with high-fidelity as shown in Fig. 33b. Then the pulse morphological parameters can be quantitatively analyzed in time domain.

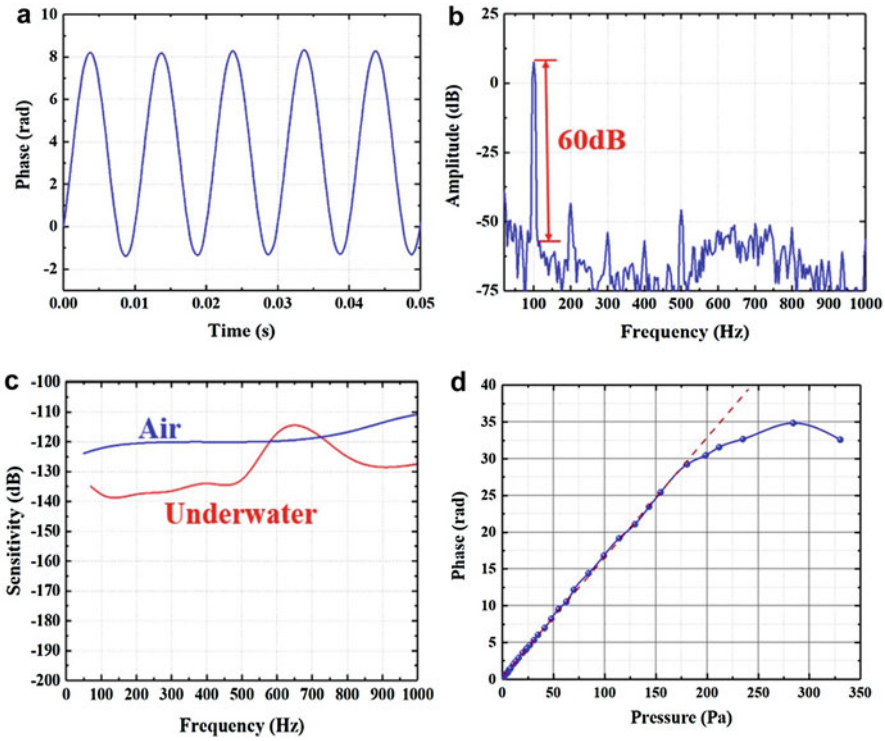

Fig. 31 Sensing performance of the polymer diaphragm-based fiber optic hydrophone: (**a**) acoustic wave recover at the frequency of 100 Hz; (**b**) frequency spectrum of the recovered signal in (**a**); (**c**) frequency responses from 50 Hz to 1 kHz when the fiber optic hydrophone was placed in air and underwater; (**d**) underwater acoustic response of the fiber optic at 100 Hz

The pulse parameters were calculated and listed in Table 1, according to the definitions in Fig. 33a. It is believed that the lower values of the parameters K, V, and AIx mean better peripheral vascular resistance, blood viscosity, and arterial compliance, respectively. Hence, the cardiovascular health conditions of subject A and B should be slightly better than C and D, though all of them stayed healthy concerning cardiovascular conditions. The pulse analysis results were consistent with the physical examination reports, preliminarily verifying the accuracy of pulse diagnosis by optical fiber sensing system and showing great potential in early cardiovascular diseases indicating.

WDM/TDM-Based Fiber Optic SPON

Except for the TDM-based SPON, hybrid WDM/TDM SPON is another mature architecture, which has higher deployment flexibility and potential larger

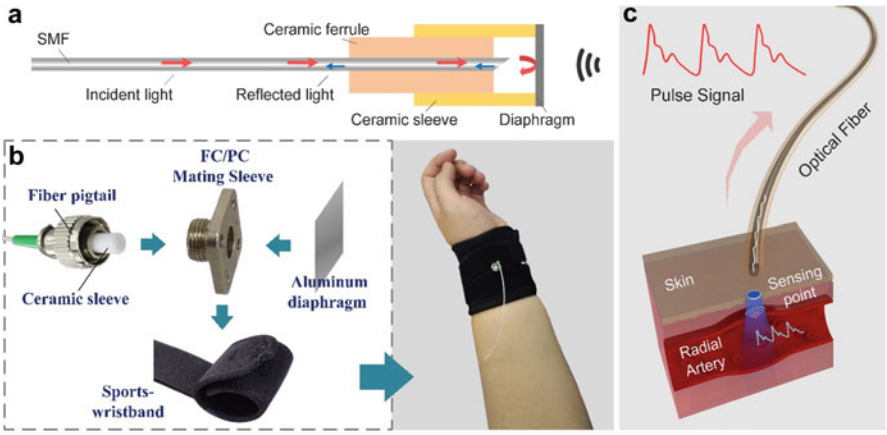

Fig. 32 (**a**) Schematic diagram of fiber optic pulse sensor; (**b**) structural design of wearable pulse sensor; (**c**) the transmission of pulse wave signals

multiplexing capacity. Here two hybrid multiplexing SPONs respectively for colored sensors and colorless sensors accessing, and their applications for micro-vibration monitoring, will be mainly discussed.

The first WDM/TDM SPON is designed for colored fiber sensors multiplexing, especially the fiber grating sensors with wavelength selectivity. Take the DBRFL sensors as the example, of which the structure, principle, as well as the networking in a single fiber have been introduced above. Actually, they can also be multiplexed in SPON to further increase the capacity. Figure 34 exhibits the schematic of the proof-of-concept sensing network, which is constructed by high-speed multi-channel optical switch (OS) for TDM and different lasing wavelengths of DBRFLs in every fiber link for WDM. Generally, the multiplexing capacity is limited by the pump budget and the switching speed of OS. In the central office, the TDM is realized by an 8 switching channels optical switch with only 100 ns switching time. The WDM is achieved by a dense wavelength division multiplexer (DWDM) with 16 wavelengths matched to channels 17–32 of C-band 200 GHz ITU grid. With the help of low pump threshold (<7.74 dBm) and low energy absorption (<0.8 dB) of the DBRFL, the 980 nm laser diode with high laser power (>28 dBm) supports serial pumping over 16 sensors. The interrogation system consists of 16 parallel demodulation channels for receiving the signals from 16 wavelength channels, and each channel can interrogate 8 channels by time-polling. Consequently, the DBRFL SPON can provide a multiplexing capacity of 128 (Liu et al. 2018).

For dynamic sensing, an interrogation system with high resolution and high response speed was developed to measure the beat frequency generated from the DBRFL sensor network. As exhibited in Fig. 35, the interrogation system consists of Radio-Frequency (RF) receiving part, digital processing part, frequency discriminator part, frequency source part, and Input/Output (I/O) part.

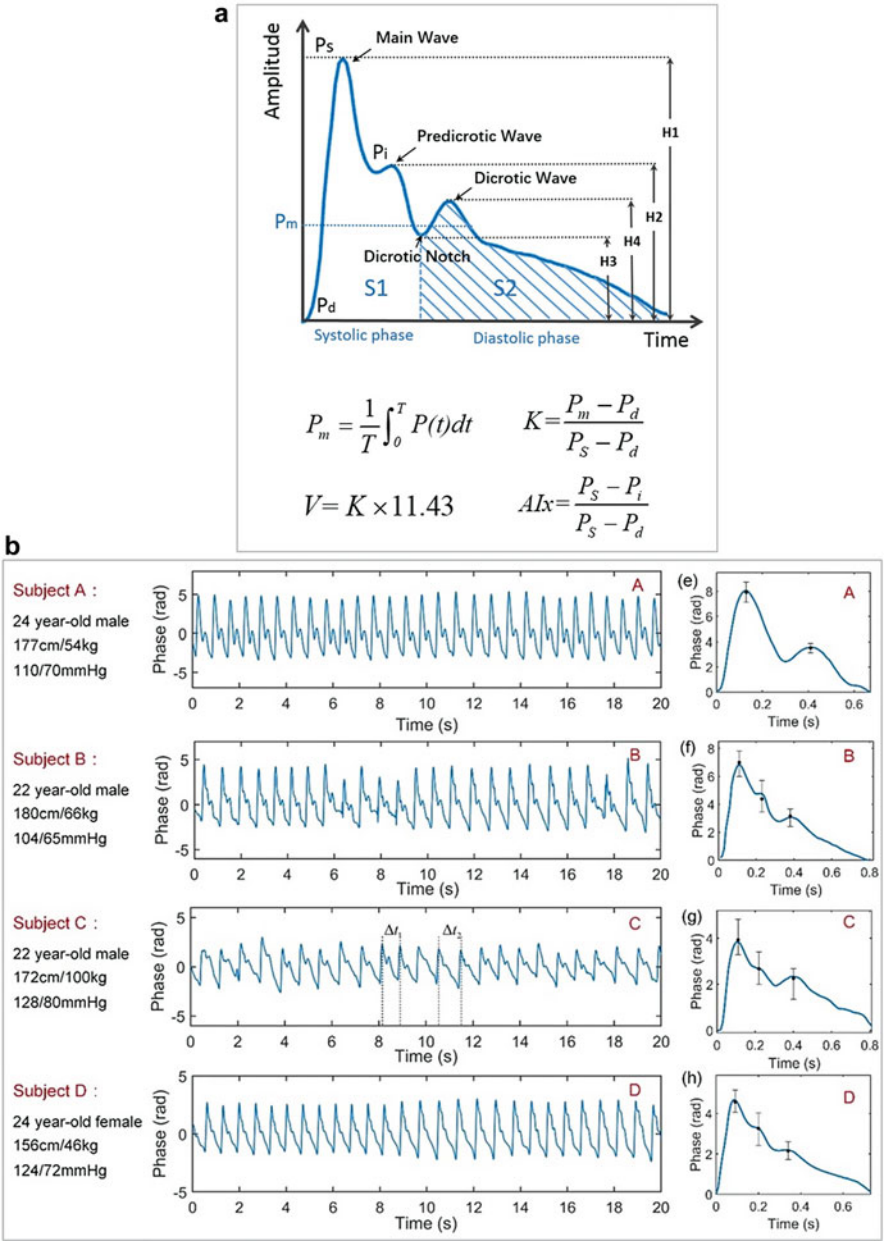

Fig. 33 (**a**) Typical waveform and assessment indicators of one pulse cycle; (**b**) pulse waveforms in 20 s (left) detected for four subjects and the statistical results in one pulse cycle (right)

Table 1 Analytical results of clinical pulse diagnosis

Indicator	Subject			
	A	B	C	D
T (s)	0.69	0.79	0.83	0.73
MBP (mmHg)	85.4	80.1	102.7	92.6
HR (bpm)	87	76	72	82
K value	0.384	0.387	0.474	0.397
V value	4.39	4.42	5.42	4.54
AIx	NA	−0.303	−0.298	−0.225

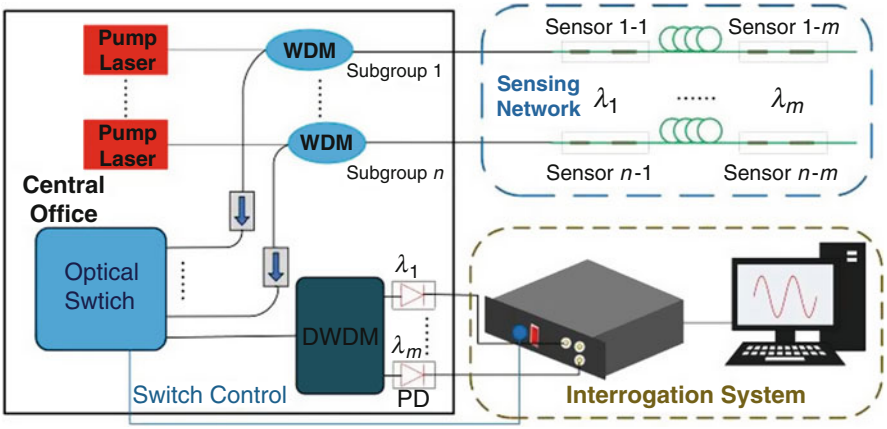

Fig. 34 Schematic diagram of the acceleration sensing network

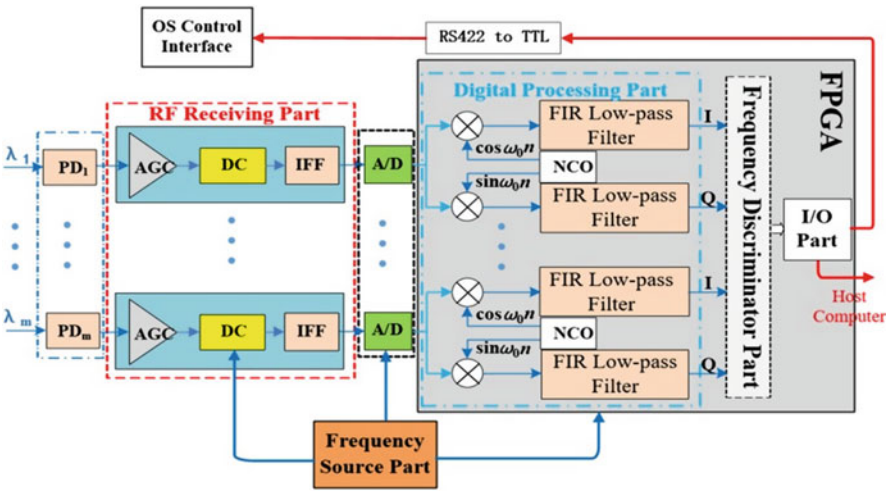

Fig. 35 Schematic of the interrogation system (*AGC* automatic gain control, *DC* down converter, *IFF* intermediate frequency filter, *NCO* numerically controlled oscillator)

The Radio-Frequency receiving part working as super-heterodyne receiver converts the original ultra-high frequency (UHF) signal to intermediate frequency (IF) signal by mixing the original signal and the local oscillator signal. Subsequently, the digital processing part mixes the digital IF signal with two orthogonal signals controlled by NCO to generate the orthogonal in-phase (I) and quadrature (Q) signals (Song 2016). Next, the frequency discriminator part extracts the frequency information from the I/Q signals through the arctangent operation and differentiator. Both the digital processing part and frequency discriminator part are realized by a high-performance FPGA (Xilinx Virtex-7) to ensure the processing speed. Beneficial from parallel demodulation of WDM channels and high switching speed of OS, the response bandwidth and frequency resolution of the interrogation system reached to DC-1 kHz and 4.7 Hz/$\sqrt{}$Hz above 10 Hz, respectively.

Based on the DBRFL SPON, a fiber optic accelerometers network was developed, by adopting the cantilever-mass transducer (Guan et al. 2010). The field test was carried out, where the tested sensors were mounted on the vibration exciter (MB Dynamic PM25) along with a commercial piezoelectric accelerometer (PCB, Inc., Model 393B31) for calibration (see Fig. 36a). The resolution of this PZT accelerometer is about 4 ng/$\sqrt{}$Hz at 100 Hz, which is the highest commercially available resolution to the best of our knowledge. The vibration exciter provides a sinusoidal vibration with adjustable frequency and amplitude. Firstly, three sensor elements were chosen to test the independence of the sensor in the network. As shown in Fig. 36b, when S12 was applied with a sinusoidal vibration at 90 Hz, while S11 and S21 were isolated the vibration, the crosstalk between S12 and S11 or S21 was lower than −70 dB. Secondly, the sensitivity and linearity of the DBRFL acceleration sensor were investigated. Taking the accelerations at 90 Hz as the example, the linear fitting result in Fig. 36c shows that the sensitivity of the sensor was 1.1604 GHz/g and the R-Square was over 0.9999. Finally, the measurement precision of the DBRFL accelerometer was tested. Theoretically, the precision is defined as the closeness of agreement between independent test results, which can be expressed by the effect of random errors on a measurement and quantified as the standard deviation of repeated measurements on the same sample using the same method (Menditto et al. 2007). Usually, Bland-Altman plot method is used to evaluate the precision (Cecconi et al. 2009). The distribution of multiple test results, illustrated in Fig. 36d, demonstrates the precision as high as 1.305 μg, which is regarded by the value of ±1.96 times of the standard deviation (95% confidence intervals) around the bias.

Another WDM/TDM SPON is served for colorless fiber optic sensors multiplexing. Figure 37a presents a typical tree topology network to access arbitrary fiber optic sensors, which is intrinsically the same as the optical fiber communication PON (Li et al. 2012b). Here, TDM is realized by employing fiber delay lines of different length in different link, and WDM is achieved through ODN (usually DWDM) connected to every OSU. The OLT of the hybrid SPON (HSPON) generates high-power, wideband pulse light, which is downward transmitted to each OSU through TDM/WDM distribution network and then receives the upward

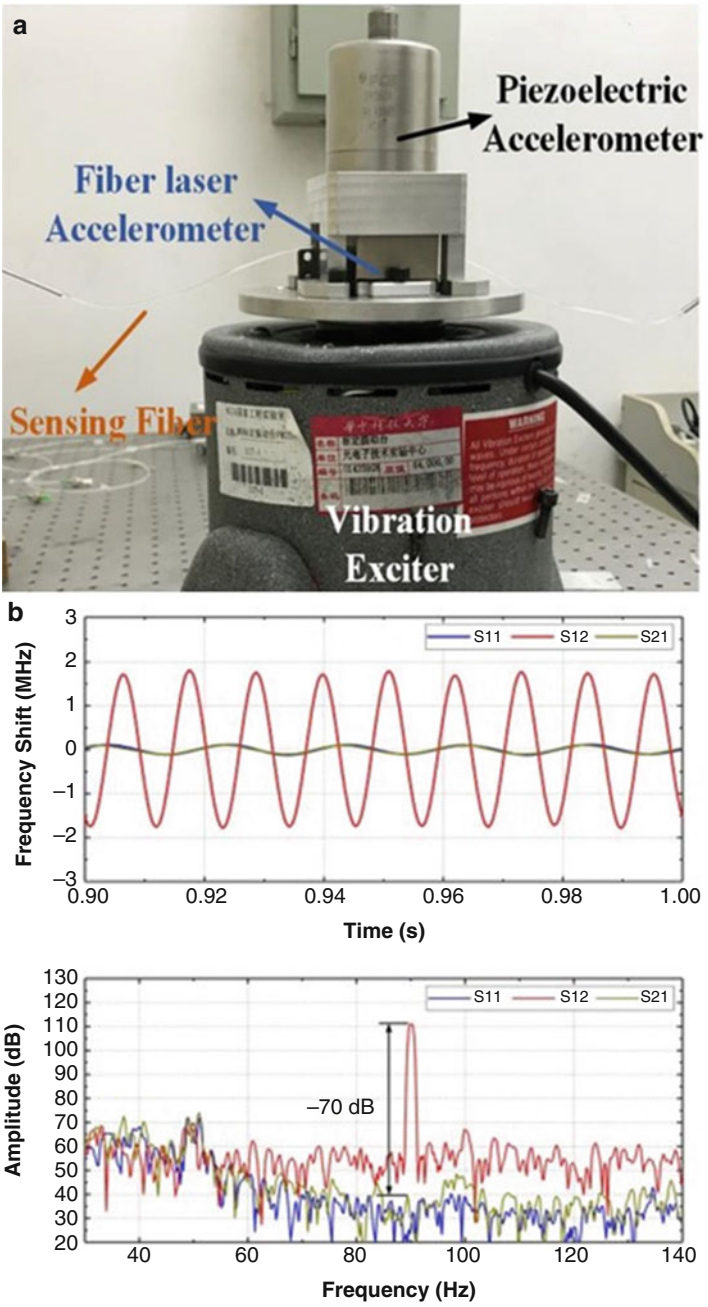

Fig. 36 (Continued)

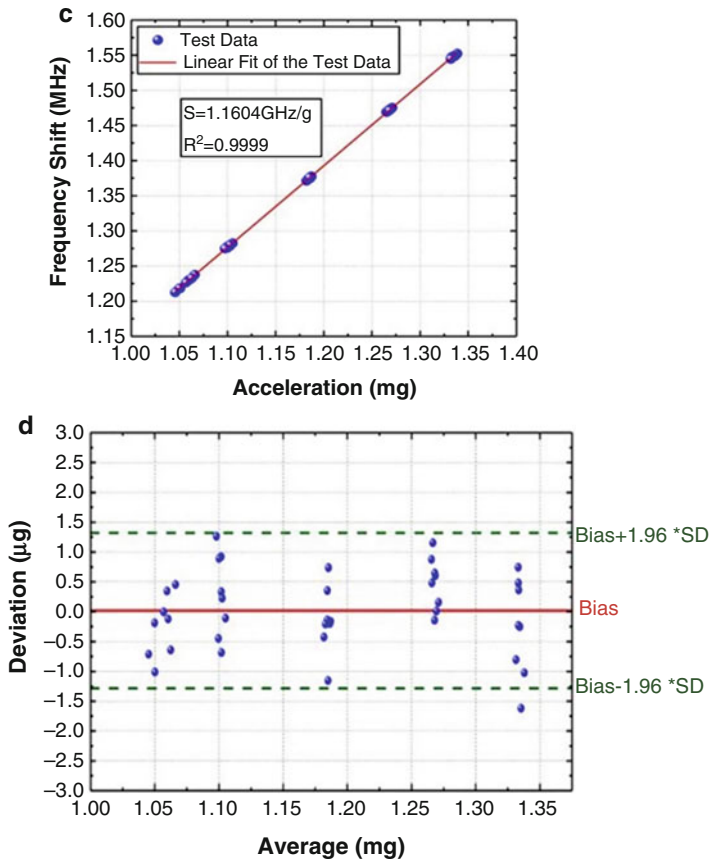

Fig. 36 (**a**) Photo of field test setup; (**b**) waveforms and frequency spectra of three sensors; (**c**) relationship between acceleration and beat frequency shift of DBRFLaccelerometer; (**d**) bland-Altman plot for DBRFL accelerometer and PZT accelerometer as reference

sensing optical signal from OSUs. The maximum capacity of the SPON is mainly determined by the spectrum bandwidth and power of light source, transmission loss of fiber link, and the channel interval of DWDM. According to the performance of the commercial devices, the capacity can reach over $8 \times 32 = 256$. In this configuration, the OSU can be interferometer-based vibration sensor, optical spectrum absorption-based gas sensor, Faraday Effect-based circulator sensor, etc., as well as flexibly deployed. Therefore, this WDM/TDM SPON can be widely utilized in many application fields such as multi-zone monitoring, multi-parameter detection, and multi-function monitoring.

A WDM/TDM SPON for perimeter intrusion detection was designed and developed. As displayed in Fig. 37b, the OSU is an unbalanced Mach-Zehnder Interferometer (MZI) followed by a Sagnac structure, which can detect the intrusion

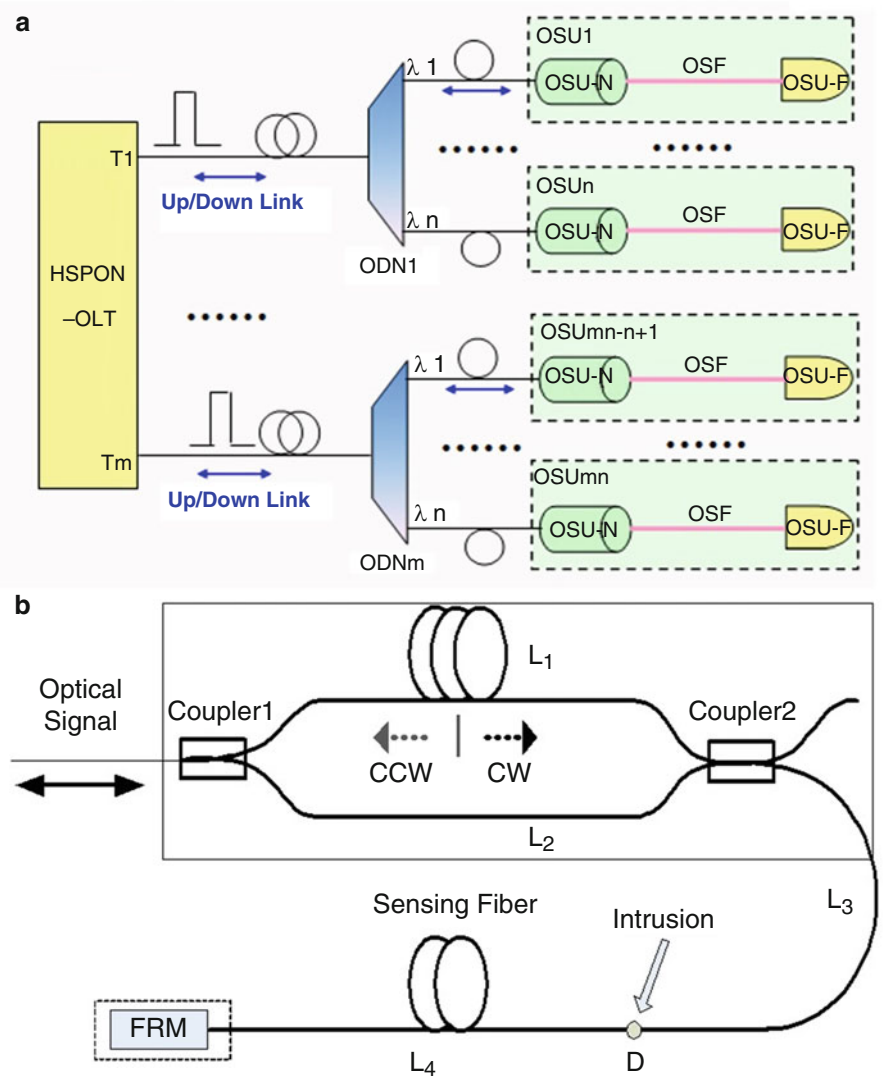

Fig. 37 Schematic of the WDM/TDM SPON for colorless interferometric sensors accessing: (**a**) architecture of the SPON; (**b**) structure of the interferometric sensor for vibration monitoring. (Copyright 2019 OSA)

in long distance without blind area. Here, the unbalanced MZI amplifies the response of intrusion in the far area and the Faraday rotation mirror (FRM) at the end of the sensing fiber is to overcome the polarization induced fading, as well as reflect the sensing signal to the OLT.

In terms of the principle discussed above, a perimeter intrusion monitoring system was explored, as illustrated in Fig. 38. The capacity of the system is 256, and the maximum sensing distance is 128 km. The fiber cable can be deployed on the ground or hung on the fence to sense the micro-vibration induced by the perimeter intrusion. The response time is less than 2 s. The missing alarm is nearly 0, due to its high sensitivity of the sensing structure, while the false alarm is only 4% benefiting from the intelligent data processing method. Different events such as walking, scrambling, and fiber cable damage can be detected and identified.

Besides, the fiber optic intrusion monitoring system can be used for cultural relics protection. Since cultural relics are usually located at remote rural areas without electricity supply, the conventional security monitoring techniques are difficult to implement it, while the fiber optic sensor presents great superiority for that. Figure 39a presents the system configuration. The host is the OLT, and the ODN is composed of WDM and TDM modules. The optical fiber micro vibration sensor is OSU, which is designed for underground condition by winding the optical fiber on the cone structure, to collect all the vibration signals near the sensor, and then transmit it to the cylinder roll protected by the intelligent materials. The field test demonstrated that the OSU can monitor the dig within the area of 25 m radius and the blasting within the area of 100 m radius. This system has been widely applied in many ancient tombs in China including Bailsman Tombs, Xianling Tombs, and so on, by deeply burying the OSUs underground (see Fig. 39b).

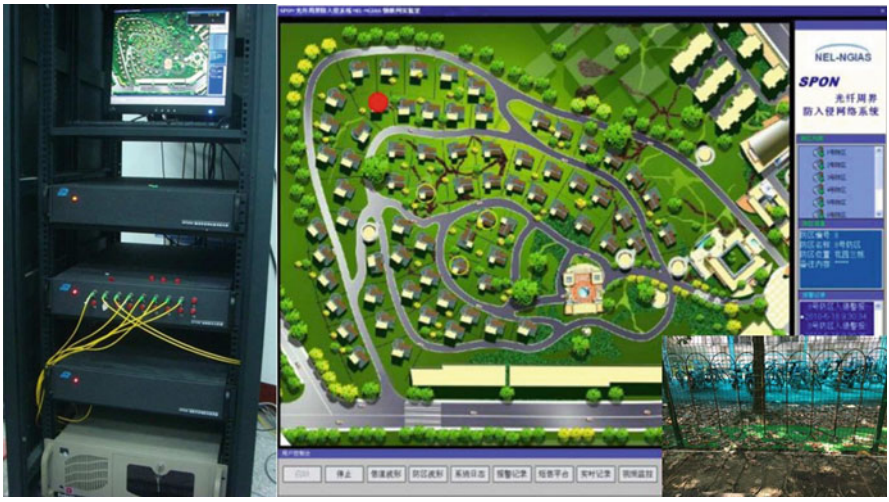

Fig. 38 Photographs of the HSPON-OLT (left) and the application software of the perimeter intrusion monitoring system (right). Inset: photo of the field test with fiber cables deployed on the ground and fence. Copyright 2019 OSA

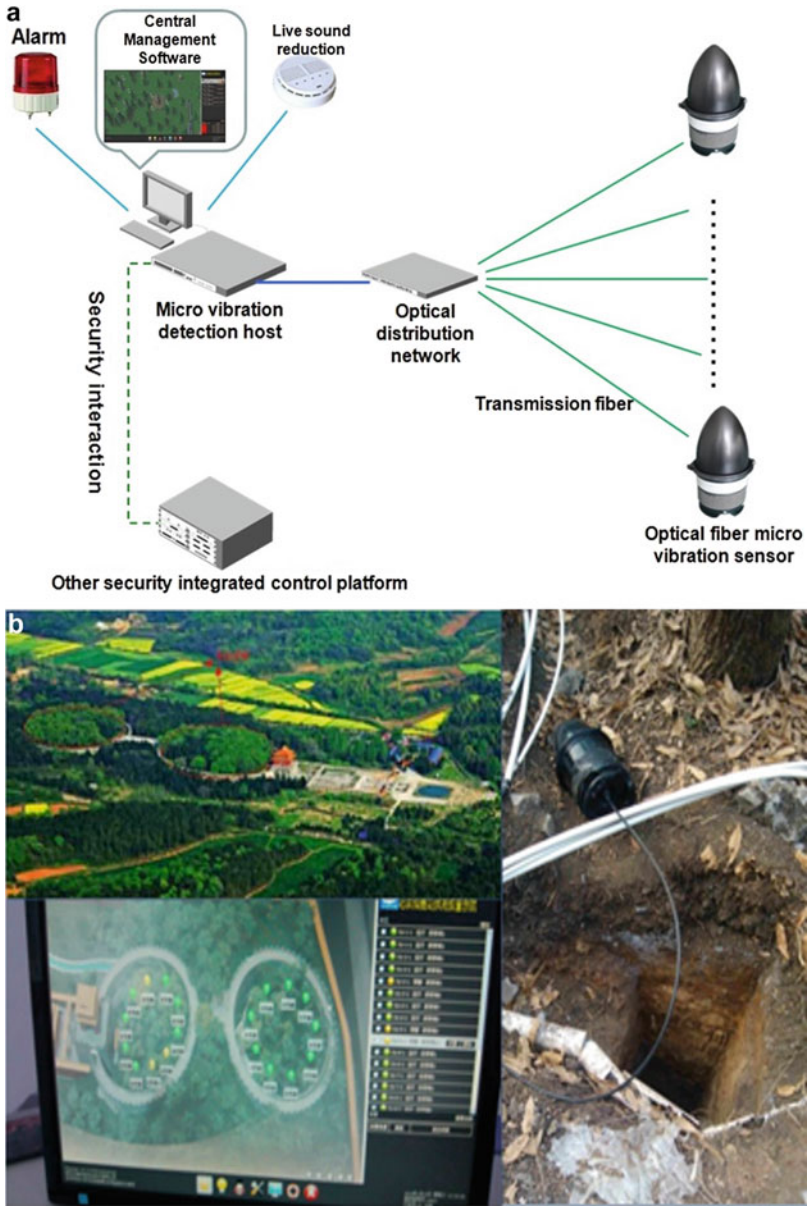

Fig. 39 (**a**) Schematic diagram of the fiber optic WDM/TDM SPON for cultural relics protection; (**b**) photograph of the field test in Xianling Tombs in China

Conclusion

In this chapter, the key technologies and industrial applications of three types of fiber optic sensor network are introduced, including the UWFBG sensor network, special fiber grating sensor network, and the fiber optic SPON. Through TDM, WDM, FDM, SDM, and their combinations, a large number of fiber optic sensors can be accessed and merged to the network. For the sensor network integrated in a single optical fiber, both quasi-distributed sensor and continuous-distributed sensor are realized by employing UWFBGs, TFGs, and DBRFLs. Moreover, the fiber optic SPON with star or tree topology provides the support of any colored or colorless fiber optic sensors accessing. The sensor structures, networking mechanisms, system architectures, demodulation methods, and typical sensing performances are systematically discussed. Besides, the developed systems or equipment for measuring the temperature, strain, acoustic, pressure, acceleration, micro-vibration, near infrared absorption, pulse wave, etc., as well as the field tests for a wide range of industrial applications such as resource exploration, geophysics, infrastructure, medical diagnose, food quality, and security control are presented. Beneficial from the large capacity, good adaptivity, and high flexibility, the fiber optic sensor network is becoming increasingly important in industrial applications, especially the sensing for large structures and surveying at complex conditions.

References

F. Ai, Q. Sun, W. Zhang, T. Liu, Z. Yan, D. Liu, in *Optical Fiber Communication Conference, OSA Technical Digest*, San Diego, California (2017)
F. Ai, H. Li, T. He, Z. Yan, D. Liu, Q. Sun, in *Optical Fiber Communication Conference, OSA Technical Digest*, San Diego, California (2018)
A.P. Avolio, M. Butlin, A. Walsh, Physiol. Meas. **31**, 1 (2009)
M. Cecconi, A. Rhodes, J. Poloniecki, A. Rhodes, Crit. Care **13**, 1 (2009)
J.W. Cheng, Q.Z. Sun, F. Ai, Y.Y. Luo, W. Zhang, X.L. Li, D.M. Liu, IEEE Photonics J. **10**, 3 (2018)
E. Cleve, E. Bach, E. Schollmeyer, Anal. Chim. Acta **420**, 143–247 (2000)
ElectroniCast Consultants (2017). https://www.electronicastconsultants.com. Accessed May 2017
R.W. Fallon, in *Doctoral Dissertation,* ed. by R.W. Fallon (Aston University, 2000), p. 18
C.Z. Fan, F. Ai, Y.J. Liu, Z.J. Xu, G. Wu, W. Zhang, C. Liu, Z.J. Yan, D.M. Liu, Q.Z. Sun, in *Optical Fiber Communication Conference, OSA Technical Digest* San Diego, California (2019)
T. Fu, Y. Liu, K.T. Lau, J. Leng, Compos. Part B-Eng. **66**, 420–429 (2014)
B.O. Guan, X.S. Sun, Y.N. Tan, in *European Workshop on Optical Fibre Sensors*, Porto, Portugal 76530Z (2010)
T. Guo, A.C. Wong, W.S. Liu, B.O. Guan, C. Lu, H.Y. Tam, Opt. Express **19**, 3 (2011)
J. Harrison, S. Foster, in *Optical Sensors 2017*, New Orleans, Louisiana (2017)
C.Y. Hu, H.Q. Wen, W. Bai, J. Lightwave Technol. **32**, 7 (2014)
M. Jamrógiewicz, J. Pharm. Biomed. Anal. **66**, 7 (2012)
L. Jin, Y.Z. Liang, M.P. Li, L.H. Cheng, J. Li, B.O. Guan, J. Lightwave Technol. **32**, 22 (2014)
P. Jousset, T. Reinsch, T. Ryberg, H. Blanck, A. Clarke, Nat. Commun. **9**, 2509 (2018)
Y. Kim, Y. Noh, K. Kim, IEEE Commun. Lett. **21**, 11 (2017)
X.L. Li, Q.Z. Sun, D. Liu, R.B. Liang, J.J. Zhang, J.H. Wo, P.P. Shum, D.M. Liu, Opt. Express **20**, 11 (2012a)

X.L. Li, Q.Z. Sun, J.H. Wo, M.L. Zhang, D.M. Liu, J. Lightwave Technol. **30**, 8 (2012b)
D.M. Liu, Q.Z. Sun, P. Lu, L. Xia, C.T. Sima, Photon. Sens. **6**, 1 (2016)
T. Liu, D.D. Lv, Y.Y. Luo, W.G. Lu, Z.J. Yan, K. Wang, C.Q. Li, D.M. Liu, Q.Z. Sun, in *Conference on Lasers and Electro-Optics*, San Jose, California (2018)
M. Manley, Chem. Soc. Rev. **43**, 24 (2014)
A. Mateeva, J. Lopez, H. Potters, J. Mestayer, B. Cox, D. Kiyashchenko, Geophys. Prospect. **62**, 4 (2014)
G.E. McVeigh, C.W. Bratteli, D.J. Morgan, C.M. Alinder, S.P. Glasser, S.M. Finkelstein, J.N. Cohn, Hypertension **33**, 6 (1999)
A. Menditto, M. Patriarca, B. Magnusson, Accred. Qual. Assur. **12**, 1 (2007)
S.V. Miridonov, M.G. Shlyagin, D. Tentori, Fiber Optic. Laser Sens. Appl. **3541**, 33–40 (1998)
S. Ni, H. Kanamori, D. Helmberger, Nature **434**, 582 (2005)
S. Samo, D.A. Carlson, D.L. Gregory, S.H. Gawel, J.E. Pandolfino, P.J. Kahrilas, Clinical Gastroenterology and Hepatology **15**, 3 (2016)
B.S. Song, in *System-Level Techniques for Analog Performance Enhancement*, ed. by B. S. S. By, (Springer, Cham, 2016), pp. 195–225
Q.Z. Sun, J.H. Wo, H. Wang, D.M. Liu, in *Proceedings of SPIE, Conference on Optical Fiber Sensors* San Diego, California (2014)
Q.Z. Sun, F. Ai, D.M. Liu, J.W. Cheng, H.B. Luo, K. Peng, Y.Y. Luo, Z.J. Yan, P.P. Shum, Sci. Rep. **7**, 41137:1–8 (2017)
M. Vidakovic, I. Armakolas, T. Sun, J. Carlton, K.T.V. Grattan, J. Lightwave Technol. **34**, 18 (2016)
Z. Wang, H.Q. Wen, C.Y. Hu, W. Bai, Y.T. Dai, Chin. Opt. Lett. **14**, 1 (2016)
J.Y. Wang, F. Ai, J.W. Cheng, W. Zhang, Z.J. Yan, D.M. Liu, Q.Z. Sun, IEEE Photonic. Tech. Lett. **30**, 18 (2018a)
J.Y. Wang, F. Ai, Q.Z. Sun, T. Liu, H. Li, Z.J. Yan, D.M. Liu, Opt. Express **26**, 19 (2018b)
J.H. Wo, M. Jiang, M.X. Malnou, Q.Z. Sun, J.J. Zhang, P.P. Shum, D.M. Liu, Opt. Express **20**, 3 (2012)
J.H. Wo, H. Wang, Q.Z. Sun, P.P. Shum, D.M. Liu, J. Biomed. Opt. **19**, 1 (2014)
T. Woodcock, C. O'Donnell, G. Downey, J. Near Infrared Spectrosc. **16**, 1 (2008)
T. Yamate, G. Fujisawa, T. Ikegami, J. Lightwave Technol. **35**, 16 (2017)
Z. Yan, C. Mou, K. Zhou, X. Chen, L. Zhang, J. Lightwave Technol. **29**, 18 (2011)
Z. Yan, A. Adebayo, K. Zhou, L. Zhang, H. Fu, D. Robinson, Opt. Photonics J. **3**, 5 (2013)
M.H. Yang, W. Bai, H.Y. Guo, H.Q. Wen, H.H. Yu, D.S. Jiang, Photonic Sens **6**, 1 (2016)
M.L. Zhang, Q.Z. Sun, Z. Wang, X.L. Li, H.R. Liu, D.M. Liu, Opt. Commun. **285**, 13–14 (2012a)
Y. Zhang, X. Xie, H. Xu, Opto-Electron. Eng. **39**, 8 (2012b)
W. Zhang, X.L. Ni, J.Y. Wang, F. Ai, Y.Y. Luo, Z.J. Yan, D.M. Liu, Q.Z. Sun, J. Lightwave Technol. (2019). Accepted to be published